iScience

CellPress
OPEN ACCESS

Article

Inhibition of a conserved bacterial dual-specificity phosphatase confers plant tolerance to *Candidatus* Liberibacter spp

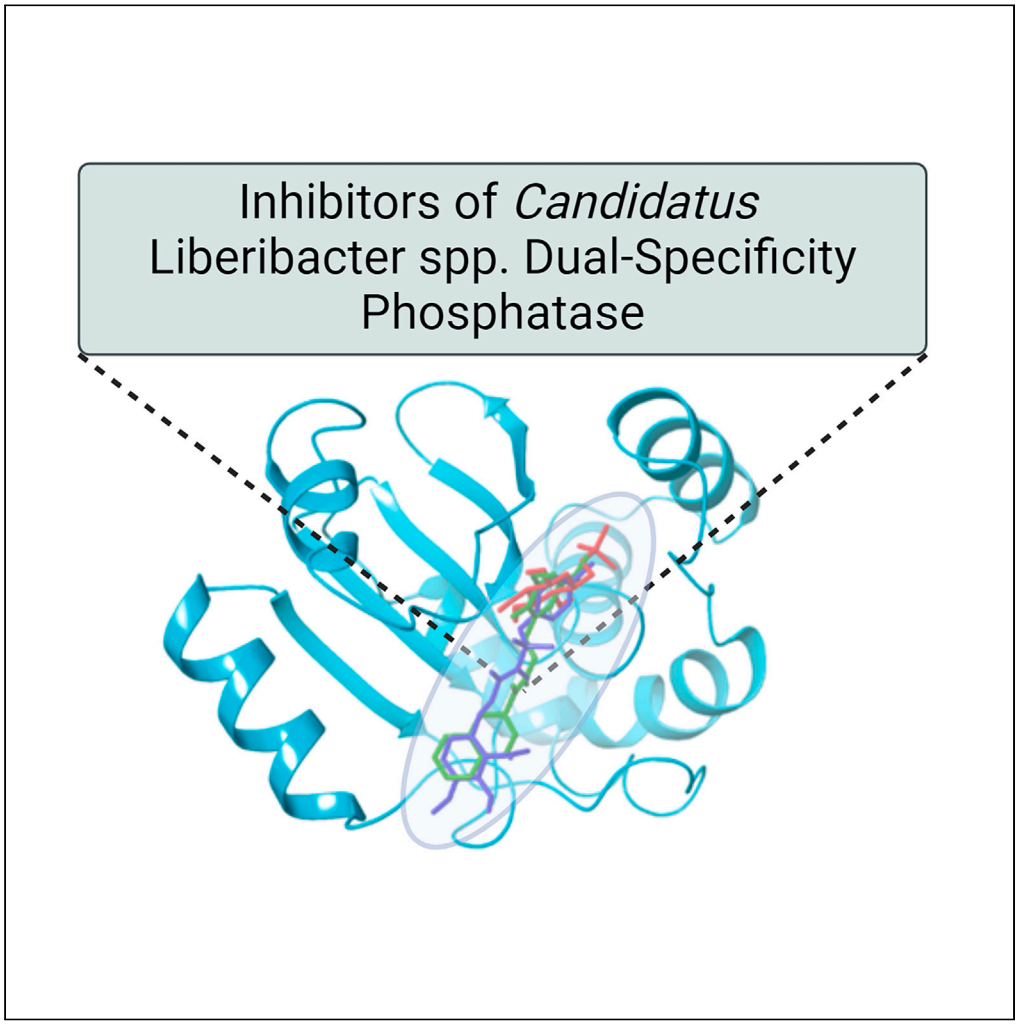

Haoqi Wang, Sonia Irigoyen, Jiaxing Liu, ..., Gitta Coaker, Sandun Fernando, Kranthi K. Mandadi

sandun.fernando@ag.tamu.edu (S.F.)
kkmandadi@tamu.edu (K.K.M.)

Highlights

A conserved protein phosphatase of "*Candidatus* Liberibacter spp." was characterized

The phosphatase interferes with plant cell death responses

Ligand screening identified two small molecule inhibitors of the phosphatase

The inhibitors conferred plant tolerance to "*Candidatus* Liberibacter spp."

Wang et al., iScience *27*, 109232
March 15, 2024
https://doi.org/10.1016/j.isci.2024.109232

iScience

CellPress
OPEN ACCESS

Article

Inhibition of a conserved bacterial dual-specificity phosphatase confers plant tolerance to *Candidatus* Liberibacter spp

Haoqi Wang,[1,8] Sonia Irigoyen,[2,8] Jiaxing Liu,[2] Manikandan Ramasamy,[2] Carmen Padilla,[2] Renesh Bedre,[2] Chuanyu Yang,[4] Shree P. Thapa,[3] Nirmitee Mulgaonkar,[1] Veronica Ancona,[4] Ping He,[5] Gitta Coaker,[3] Sandun Fernando,[1,*] and Kranthi K. Mandadi[2,6,7,9,*]

SUMMARY

"Candidatus Liberibacter spp." are insect-vectored, fastidious, and vascular-limited phytopathogens. They are the presumptive causal agents of potato zebra chip, tomato vein clearing, and the devastating citrus greening disease worldwide. There is an urgent need to develop new strategies to control them. In this study, we characterized a dual-specificity serine/tyrosine phosphatase (STP) that is well conserved among thirty-three geographically diverse "*Candidatus* Liberibacter spp." and strains that infect multiple Solanaceaea and citrus spp. The STP is expressed in infected plant tissues, localized at the plant cytosol and plasma membrane, and interferes with plant cell death responses. We employed an *in silico* target-based molecular modeling and ligand screen to identify two small molecules with high binding affinity to STP. Efficacy studies demonstrated that the two molecules can inhibit "*Candidatus* Liberibacter spp." but not unrelated pathogens and confer plant disease tolerance. The inhibitors and strategies are promising means to control "*Candidatus* Liberibacter spp."

INTRODUCTION

Several devastating plant diseases are caused by fastidious (unculturable) "*Candidatus* Liberibacter spp." For instance, potato zebra chip disease, caused by "*Candidatus* Liberibacter solanacearum" (CLso), leads to millions of dollars in losses to the potato industry.[1] Similarly, citrus greening or Huanglongbing (HLB) disease, caused by "*Candidatus* Liberibacter asiaticus" (CLas), is the most devastating disease of citrus today and threatens citrus production worldwide. HLB is transmitted by an insect vector, the Asian citrus psyllid (*Diaphorina citri*). Since its inception in 2006, in Florida alone, HLB caused a ≥50% reduction in citrus acreage and economic losses upwards of US $8 billion.[2,3]

The citrus industry is evaluating multiple antibiotic-based therapies to control "*Candidatus* Liberibacter spp." Between the 1970s and 1980s, tetracycline, penicillin, and other antibiotics were tested for HLB suppression in citrus.[4–6] Trunk applications of penicillin and oxytetracycline in symptomatic sweet orange trees provided tolerance, tree health, and yield improvements.[4,7,8] In a drastic measure to control HLB, the Florida citrus industry has obtained a Section 18 emergency exemption from the Environmental Protection Agency (EPA) to use commercial antibiotic/bactericide products. Some products (e.g., ArborOTC, Firewall^{TM,} and FireLine) have been commercially used in Florida over the last few years.[7–9] Although promising in the short term, these bactericides are also being used in animal and human medicine,[10] and their extensive deployment in agriculture in the long term poses threats to the emergence of antibiotic resistance.[11] Thus, there is a need to explore alternative therapies for disease management by advancing knowledge of the "*Candidatus* Liberibacter spp." pathosystem and employing interdisciplinary approaches.

Target-based molecular modeling and ligand screening are commonly employed in biomedical and pharmaceutical research to discover new drugs and inhibitors.[12] Fewer studies have used this approach in plant-microbial interactions and are limited to the studies of plant proteins.[13,14] Here, we characterize a "*Candidatus* Liberibacter spp." dual-specificity serine/tyrosine phosphatase (STP), conserved among 33 "*Candidatus* Liberibacter spp." strains, and functions to interfere with host cell death responses. Using *in silico* molecular modeling and

[1]Biological and Agricultural Engineering Department, Texas A&M University, College Station, TX, USA
[2]Texas A&M AgriLife Research & Extension Center, Texas A&M University System, 2415 E. Highway 83, Weslaco TX 78596, USA
[3]Department of Plant Pathology, University of California, Davis, Davis, CA, USA
[4]Department of Agriculture, Agribusiness, and Environmental Sciences, Texas A&M University-Kingsville, Citrus Center, Weslaco, TX, USA
[5]Department of Biochemistry and Biophysics, Texas A&M University, 2128 TAMU, College Station, TX, USA
[6]Department of Plant Pathology and Microbiology, Texas A&M University, 2132 TAMU, College Station, TX, USA
[7]Institute for Advancing Health Through Agriculture, Texas A&M AgriLife, College Station, TX, USA
[8]These authors contributed equally
[9]Lead contact
*Correspondence: sandun.fernando@ag.tamu.edu (S.F.), kkmandadi@tamu.edu (K.K.M.)
https://doi.org/10.1016/j.isci.2024.109232

ligand screening approaches, we further identify two pharmacophore-based inhibitors of STP that demonstrated significant antimicrobial activity against "*Candidatus* Liberibacter spp." in plant tissues.

RESULTS AND DISCUSSION

STP is a conserved dual-specificity phosphatase encoded by diverse strains of *Candidatus* Liberibacter spp

A prior proteomics analysis annotated a unique dual-specificity phosphatase (CLIBASIA_03975, hereafter referred to as serine/tyrosine phosphatase, STP) and classified it as a putative virulence protein based on the absence of detectable homologs in other organisms, which is indicative of rapid evolution.[15] Phylogenetic analysis of 88 protein-coding genes from 33 bacterial genome datasets suggests that *C*Lso and *C*Las genomes are evolutionarily closer to each other than other bacterial species.[16,17] We further compared the genomes of multiple *C*Lso and *C*Las strains[17] to analyze their STP sequences. STP was present and conserved among geographically diverse *C*Lso and *C*Las strains (Figures 1A and 1B), sharing ≥69% amino acid similarity (55% identity) between *C*Lso and *C*Las isolates (Figure 1A). Phylogenetic analyses also reveal a high degree of conservation of STP genes within *C*Lso and *C*Las isolates (Figure 1B). For instance, the STP protein shares ≥95% amino acid similarity within *C*Lso isolates (Figure S1A) and ≥99% amino acid similarity within *C*Las isolates (Figure S1B). Expression analysis of infected plants confirmed STP presence and expression in *C.* Liberibacter-infected potato and citrus shoots (Figure 1C). Next, we evaluated whether *C*Lso and *C*Las STP possess phosphatase activity. The respective coding sequences were cloned into binary vectors and expressed in *Arabidopsis thaliana* protoplasts as HA-tag fusions, followed by immunopurification using anti-HA beads. Enzymatic activity of the immunopurified *C*Lso and *C*Las STP and a non-phosphatase protein control (GFP) control were determined using a *p*-nitrophenyl phosphate (pNPP)-based substrate assay.[18] Both *C*Lso and *C*Las STPs demonstrated robust phosphatase activity (Figure 1D). Together, these results indicate that STP is a conserved and active phosphatase expressed in *C.* Liberibacter-infected plant tissues.

STP localizes to the host cytosol and plasma membrane and attenuates Prf^{D1416V}-mediated plant cell death response

C. Liberibacter spp. is an obligate and intracellular pathogen. We next sought to determine the sub-cellular localization of STP in plant cells. For this, *C*Las STP was selected and tagged with a green fluorescent protein at the C-terminus (STP::GFP) and transiently overexpressed in grapefruit protoplasts. Fluorescence imaging showed accumulation of STP::GFP primarily in the cytosol and plasma membrane (Figure 2A). STP::GFP was also localized to a few unidentified cytosolic structures, possibly mitochondria or vesicles. These data support a model wherein STP could interfere with host cellular proteins and processes.

Little is known about the functions of bacterial-encoded dual-specificity phosphatases. In humans, multiple dual-specificity phosphatases have demonstrated activity toward MAP-kinases (MAPKs) and mediate positive and negative cellular immune and inflammation responses.[19] The dual-specificity phosphatases were also active targets in drug design for fighting diseases, cancer, and inflammation therapies.[19] Given the significance of MAPK activations, phosphorylation, and dephosphorylation events in general during plant-pathogen interactions and signal transduction, we evaluated whether STP could interfere with plant immune responses. We utilized a well-established transient Prf-mediated cell death genetic assay.[20,21] Prf is a tomato NBARC-LRR resistance (R) protein that confers resistance to *Pseudomonas syringae* pv. *tomato* (Pst). Prf^{D1416V} is an autoactivated kinase mutant of Prf with single amino acid substitution at D1416 in the isoleucine-histidine-aspartic acid (IHD) motif that triggers a hypersensitive response (HR)-like programmed cell death (PCD) or lesions in plants in a pathogen or effector-independent manner.[20,21] The PCD phenotype was further quantitated by a scoring scale of 0 (no lesions), 0.5 (moderate lesions), and 1 (strong lesions) using five independent biological replicates.[20] Potential effectors or inhibitors of cell death can be examined by screening for suppressing Prf^{D1416V} -induced cell death. STPs encoded in a binary expression vector were co-infiltrated with Prf^{D1416V} in *N. benthamiana* (Figures 2B and 2C). Leaves infiltrated with Prf^{D1416V} alone, Prf^{D1416V} + empty vector (EV), and mock infiltrations were used as controls. As expected, Prf^{D1416V}alone and EV infiltration induced prominent lesions by 15 dpi (Figures 2B and 2C). In contrast, leaves co-infiltrated with Prf^{D1416V} + *C*Las or *C*Lso STP showed a significant reduction of lesions (Figures 2B and 2C), similar to mock-infiltrated leaves (Figures 2B and 2C).

Molecular dynamic simulation identifies binding hotspots on STP tertiary structure

Genetic manipulation of *C.* Liberibacter spp. and its encoded proteins is not feasible due to their unculturable and obligatory lifestyle. Hence, we explored alternative approaches to block STP activity in planta. Target-based molecular modeling and ligand screening are commonly employed in biomedical and pharmaceutical research for drug discovery.[12] Fewer studies have employed this approach in plant-microbial interactions and are limited to studies of plant proteins.[13,14] To use these tools for identifying *C.* Liberibacter spp. inhibitors, we first generated homology models of *C*Lso and *C*Las STPs, using experimentally determined structures of a protein template in the protein database bank.[22] The homology model was built based on the template protein (PDB: 4RKK[23]) using SWISS-MODEL via the HHblits protein sequence search package while enabling the highest sequence coverage and identity.[24] This selected template was a phosphatase with a carbohydrate-binding domain and a dual-specificity phosphatase domain. Glucose-6-phosphate (G6P) was used as a reference substrate to represent the phosphate ions and α-D-glucose native substrates. Both *C*Lso and *C*Las STP structures overlapped on residue 40 to 191 with a 0.72 coverage rate and 0.29 sequence identity rate (Figure 3A). Visual molecular dynamics (VMD)[25] was used to depict the structural differences between the homology model *C*Lso STP and *C*Las STP (Figure 3). Sequence alignment showed a homology value (QH) of 0.9563, root-mean-square deviation (RMSD) of 0.6389 Å, and percent identity of 62.5 which suggested that the two proteins had a high degree of structural similarity, in line with the multiple sequence alignment results (Figure 1). The two homology models had a good overlap on various substrate-binding domains with the template. Next, we identified binding hotspots (pharmacophores) using the *C*Lso STP protein model. Identification of primary and

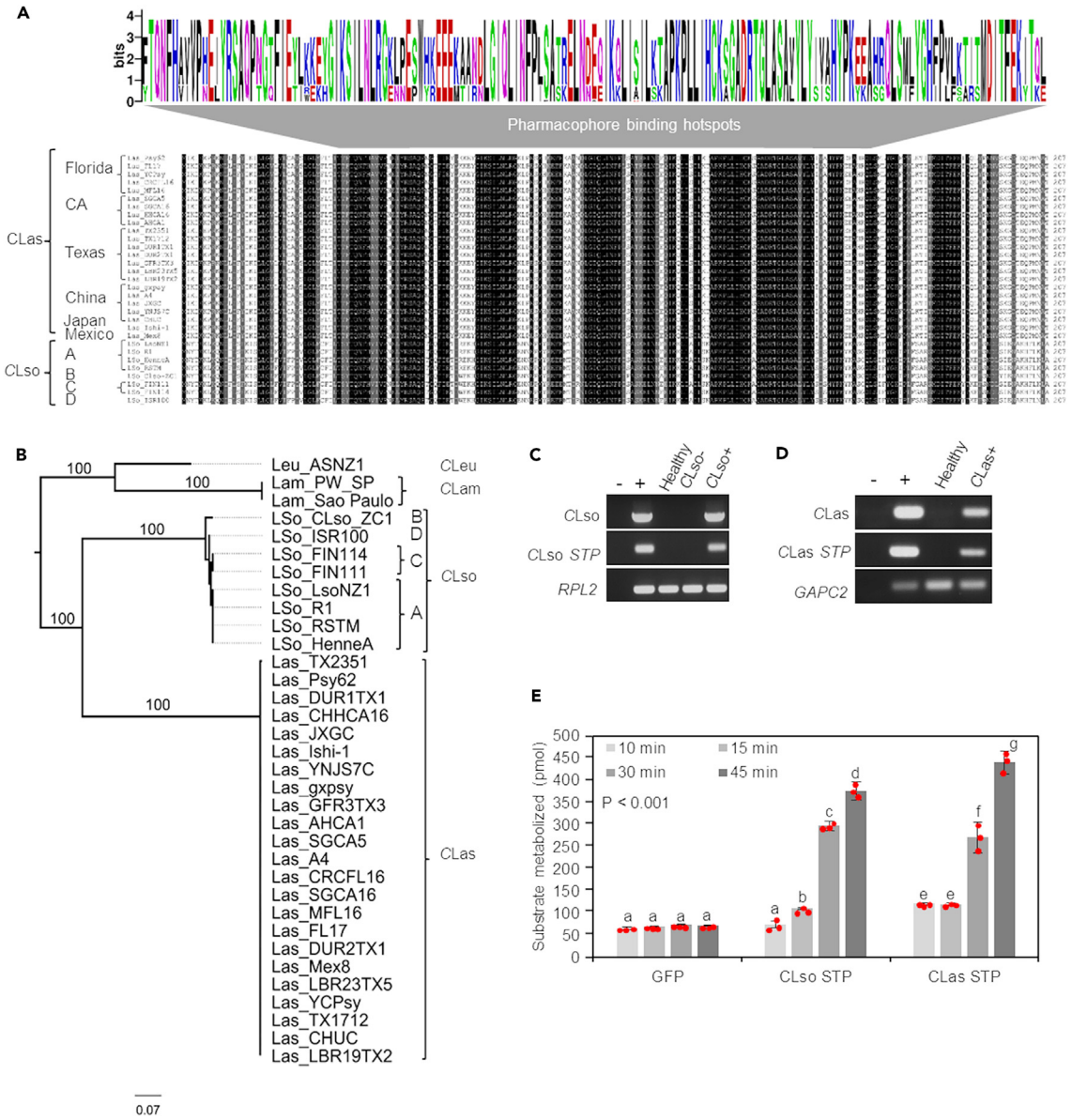

Figure 1. A conserved serine/tyrosine phosphatase (STP) encoded by multiple "*Candidatus* Liberibacter spp."

(A) Multiple sequence alignment and (B) phylogenetic relationships of the putative conserved serine tyrosine phosphatase (STP) encoded by "*Candidatus* Liberibacter solanacearum" (*C*Lso), asiaticus (*C*Las), europaeus (*C*Leu), and americanus (*C*Lam) strains isolated and sequenced from diverse geographical locations. Identical amino acids (100% conserved sequence) across all strains are shaded in black, while similar residues are shaded in gray. Residues that lack similarity across 1 or more isolates are shaded white. Pharmacophore/binding hotspot regions are shown in the sequence logo. Enlarged sequence alignments are presented in Figure S1. The maximum likelihood method and 1,000 bootstrap replicates were employed to construct the unrooted phylogenetic tree.

(C) Expression of *STP* in leaves of healthy potatoes or challenged with psyllids carrying *C*Lso+ or not (*C*Lso-).

(D) Expression of *STP* in leaves of healthy citrus or citrus infected with *C*Las+. Lanes "-" and "+" are negative (no template) and positive controls, respectively. Uncropped raw agarose gel images used to prepare e and f are presented in Figure S9.

(E) Phosphatase activity assays of *C*Lso and *C*Las STPs. The amount (pmols) of substrate metabolized by *C*Lso STP and *C*Las STP, compared to the GFP protein control, over 45 min of reaction time. Statistically significant differences were determined with one-way ANOVA followed by Tukey's honestly significant difference (HSD) test. Different lowercase letters represent significant differences among the group means ($p \leq 0.05$). p value of ANOVA is indicated. Data are represented as mean ± SEM.

allosteric (if present) substrate-binding site(s) of STP was initially approximated via Autodock Vina,[26] followed by in-depth analyses via nano-scale molecular dynamics (NAMD)[27] simulations and Drugui.[28] The goal was to accurately identify binding features in an environment resembling what the enzyme would encounter *in vivo*. NAMD combined Drugui was used to determine the binding features by sending multiple

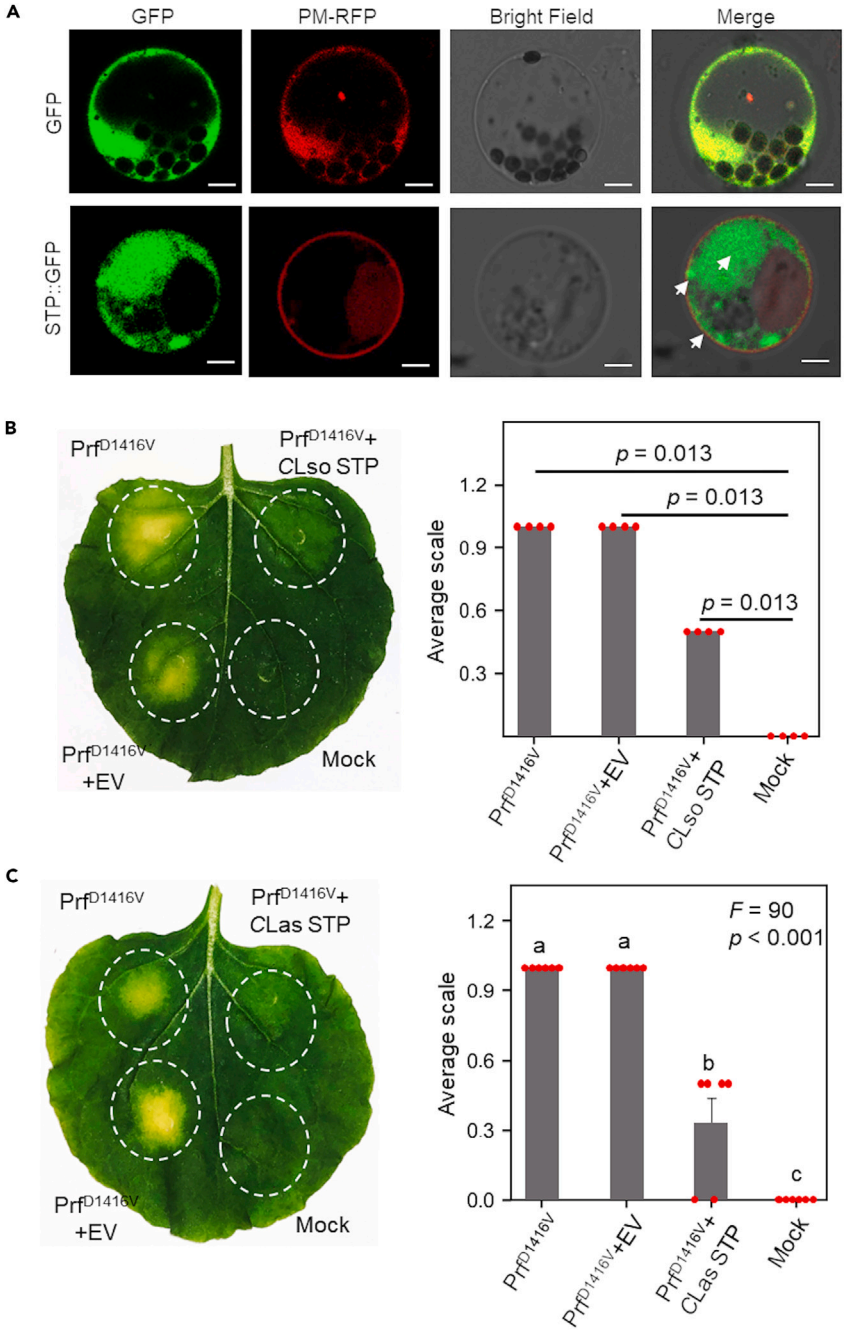

Figure 2. STP accumulates in plant cytosol and plasma membrane and suppresses Prf^{D1416V}-induced plant cell death

(A) Subcellular localization of STP. Grapefruit protoplasts were transfected with full-length CLas STP::GFP encoding binary vector. A plasma membrane (PM) marker gene tagged with red fluorescent protein (RFP, PM-RFP) was co-transfected to indicate PM. After 24 h, protoplasts were observed using a confocal laser-scanning microscope. STP::GFP and PM localization is indicated by green and red fluorescence signals, respectively. Overlapping green and red signals are shown in the third panel. Arrowheads point to the STP localization in the cytosol, plasma membrane, and a few unidentified organelles, possibly mitochondria.

(B and C) Transient expression of the *C*Lso and *C*Las STP peptides suppresses Prf^{D1416V}-induced cell death in *N. benthamiana*. *Agrobacterium tumefaciens* carrying binary expression vectors with either *C*Lso or *C*Las STP were co-infiltrated with Prf^{D1416V} containing plasmid in *N. benthamiana* leaves, along with Prf^{D1416V}alone, empty vector control (EV) or mock-infiltrated (Mock) controls. Prf^{D1416V}-induced cell lesions phenotype was assessed at 15 dpi. Representative images are shown in B and C (left panels). Quantification of the data shown in the graphs (right panels) was done by scoring the cell lesion phenotypes of five independent biological replicates as follows: 0 = no lesions, 0.5 = moderate lesions, and 1 = strong lesions. Data are represented as mean ± SEM (n = 5). Statistically significant differences in b were determined by the Kruskal-Wallis test followed by the Mann-Whitney U test for comparing treatments with the mock. p values of Mann-Whitney U tests are indicated. Statistically significant differences in c were determined using one-way ANOVA followed by Tukey's HSD test. Unlike lowercase letters represent significant differences among the group means ($p \leq 0.05$). F and p values of ANOVA are indicated. Data are represented as mean ± SEM.

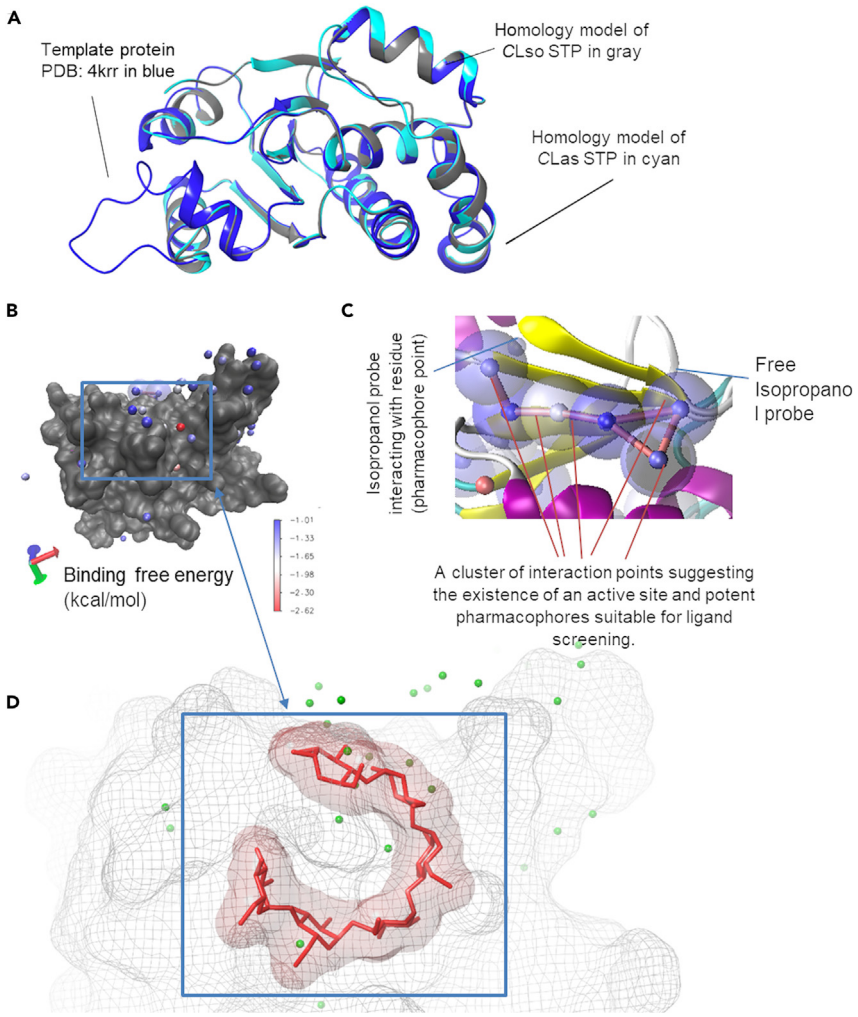

Figure 3. Homology modeling of *CLso* and *CLas* STP and identification of binding hotspots

(A) The homology model of *CLso* STP (gray) and *CLas* STP (cyan) is overlaid with the template (PDB ID: 4RKK in blue).

(B) Hotspot distribution when NAMD simulations were performed with select probes on the *CLso* STP enzyme. The red spot depicts a binding hotspot with the highest affinity. The area demarcated by the red box depicts pharmacophore distribution at the primary site.

(C) Multiple pharmacophores were clustered around the *CLso* STP enzyme, implying potential binding site(s).

(D) The selected pharmacophores (green) occupied a binding pocket in the *CLas* STP (gray mesh), consistent with the experimental substrate analog alpha-maltohexaose (red).

types and quantities of selected ligands to the dynamically changing receptor. To mimic the cytosolic environment *in silico*, the protein was immersed in a water sphere in the presence of different concentrations of the ligand(s). Each system was minimized and simulated to discern the hotspots where ligand(s) preferentially bound while the protein was still undergoing structural motions. Once the hotspots were identified, the binding features and locations (in 3D space) were recorded as pharmacophore points. From this, we identified at least sixty-seven potential binding hotspots (Figure 3B), with binding energies varying between −1.01 and −2.62 kcal/mol. The acetate drug-like probe had the highest binding affinity of −2.62 kcal/mol, and the site where acetate was bound was considered an active site. The interaction points that participate in substrate binding were further isolated by identifying clusters where several high-affinity hotspots lie closer, suggesting an active site (Figure 3C) (Table S3). The *CLas* STP pharmacophore clusters, the G6P substrate, and the template/homology model (PDB: 4RKK[22]) were overlapped to determine whether the pharmacophores generated were in the active site. The protein-ligand structures after alignment showed that the selected *CLas* STP active site coincided with the dual specificity phosphatase (DSP) domain on laforin (Figure 3D).

In silico ligand screening identified competitive inhibitors of STP

Ligand screening was performed *in silico* by pooling the features of both the ligand (via Autodock) and the receptor pocket (NAMD/Drugui) using ELIXIR-A.[29–31] This hybrid approach allowed the screening of a pool of pharmacophore features orders of magnitude larger than those

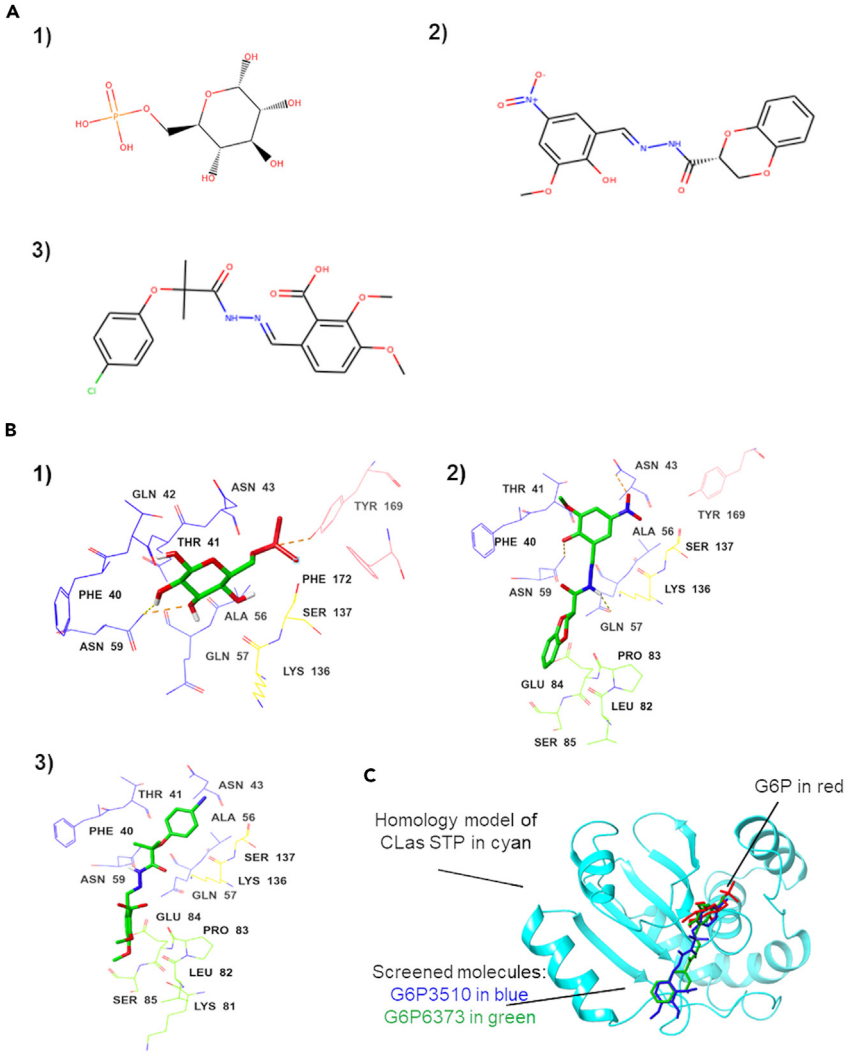

Figure 4. Identification of competitive inhibitors (G6P3510 and G6P6373) that bind to *C*Las STP

(A) structural information of the screened compounds; (1) a native enzyme substrate G6P; (2) Screened inhibitor G6P6373; (3) Screened inhibitor G6P3510.

(B) The interactions of STP with G6P, G6P6373, and G6P3510, respectively.

(C) G6P (red) occupies the active site, and an isolated ligand (blue) occupies the same site as G6P on *C*Las STP (cyan).

that would have been possible when using either the ligand or pocket alone. The previous approach would allow for deciphering more effective and site-specific inhibitors. The zincpharmer algorithm was used to sift through a library of compounds for possible hits that match the identified pharmacophore with potential inhibitors.[32] Lipinski's rule of five and high pharmacophore scores in zincpharmer were used to narrow down the hits.[33] The screening efforts isolated two potential candidates with higher affinities (G6P3510, −5.38 ± 0.379 kcal/mol and G6P6373, −5.41 ± 0.438 kcal/mol) to the active binding site on *C*Lso STP than a native substrate, glucose-6-phosphate (G6P, −4.74 ± 0.196 kcal/mol) (Table 1) (Figure 4A1–3; Figure S2A1–3). G6P is a primary metabolite in the cell that is fundamental to numerous biochemical processes and was used as a native substrate for the phosphatases. Both the inhibitors conformed with Lipinski's rule of five, which defines properties necessary for good permeation[34] (Table 1). Based on the octanol-water partition coefficient (logP) analysis, G6P was likely to be hydrophilic, while G6P3510 and G6P6373 were hydrophobic due to aromatic groups. Furthermore, the G6P substrate appeared to have a higher bioactivity score (1.23) when compared to the two screened compounds (−0.19 and −0.54) (Table 1). Interestingly, the two compounds had distinct structures and functional groups, although they were predicted based on similar pharmacophores compared to the original substrate G6P. This underscores the value of large-scale screening of *in silco* chemical databases to identify unique chemistries or interactions.

For any ligand to be an effective drug (i.e., an inhibitor), it is essential that, after binding, the ligand blocks any possibilities for the enzyme-substrate to bind to the enzyme. This could happen only if the ligand binds more strongly to the pocket than the substrate and if the ligand occupies a vast majority of possible binding sites that would otherwise be available for the substrate to bind. Thus, it is critically important that the substrate-binding site(s) and inhibitor-binding site(s) overlap. Accordingly, the nature of interactions was deciphered via Autodock Vina

Table 1. Structural and functional information of potential inhibitor ligands with G6P control

Compound name	Glucose 6-phosphate	G6P3510	G6P6373
InChI Key	NBSCHQHZLSJFNQ-DVKNGEFBSA-N	FNDOMYALHUMMDS-SSDVNMTOSA-N	GKLIPLBJOGUXHG-QGMBQPNBSA-N
Octanol-water partition coefficient logP	−3.31	3.90	−0.87
molecular weight (Daltons)	260.13	420.85	373.31
number of hydrogen bond acceptors	9	8	10
number of hydrogen bond donors	6	2	1
"Rule of five" violations	1	0	0
Number of Rotatable Bonds	7	8	5
Enzyme inhibitor score[a]	1.23	−0.19	−0.54
Average docking affinity on *C*Lso STP, kcal/mol ± std (n = 10)	−4.74 ± 0.196	−5.38 ± 0.379	−5.41 ± 0.438
Average docking affinity on *C*Las STP, kcal/mol ± std (n = 10)	−4.38 ± 0.379	−5.30 ± 0.283	−5.27 ± 0.320

[a]The enzyme inhibitor score is one of the drug-likeness & bioactivity score provided by Molinspiration.

docking simulation, this time in the presence of substrate(s) and potential inhibitor(s) on respective enzymes. Autodock Vina binding confirmations showed that the substrate and inhibitors had similar contact residue groups on *C*Lso STP (Figure S2B). G6P formed van der Waals interactions with residues Asn 43 while forming hydrogen bonding with Tyr 160 and Thr 41 (with a distance of 1 Å). G6P3510 formed van der Waals interactions with residues Tyr 40, Asn 43, and Gln 57 while forming hydrogen bonding with Thr 41 (with a distance of 1 Å). G6P6373 formed van der Waals interactions with residue Thr 59 while forming hydrogen bonding with Tyr 40 and Thr 41 (with a distance of 1 Å). In a manner similar to the *C*Lso STP interactions, the two inhibitors, G6P3510 and G6P6373, also displayed high binding affinities of −5.30 ± 0.283 kcal/mol and −5.27 ± 0.320 kcal/mol, respectively, vs. −4.38 ± 0.379 kcal/mol for G6P to the active binding site on *C*Las STP (Table 1) (Figure 4B1–3). The substrate and inhibitors showed similar contact residue groups on CLas STP (Figure 4C). G6P formed van der Waals interactions with residues Tyr 169 and Phe 40 while forming hydrogen bonding with Thr 41, Asn 43, and Asn 59 (with a distance of 1 Å). G6P3510 formed van der Waals interactions with residues Lys136, Asn 43, Glu 84, and Ser 85 while forming hydrogen bonding with Asn 59 (with a distance of 1 Å). G6P6373 formed van der Waals interactions with residue Phe 40, Gln 57, Asn 59 Pro 83, Ser 85, and Lys 136 while forming hydrogen bonding with Asn 43 and Thr 41 (with a distance of 1 Å). In summary, the *in silico* simulations identified multiple potential interactions between inhibitors and the STP proteins.

G6P3510 and G6P6373 interact with STPs via multiple intermolecular hydrogen bonds

MD simulations were performed to validate the performance and stability of the two small molecules in the binding pocket. The G6P/*C*Las STP, G6P3510/*C*Las STP, and G6P6373/*C*Las STP complexes were simulated for 100 ns to find the conformational changes within the active site. RMSD and root-mean-square fluctuations (RMSF) of the structures were used to determine whether the system had reached equilibrium during the simulation. The RMSD changes of G6P/*C*Las STP, G6P3510/*C*Las STP, and G6P6373/*C*Las STP complexes were analyzed to evaluate the stability of each complex during 100 ns MD simulations (Figure S3A). All three complexes plateaued after 20 ns of simulation and remained in the range of 2.5 Å to 4 Å. The final RMSDs were 3.082 Å, 3.683 Å, and 2.972 Å for G6P/*C*Las STP, G6P3510/*C*Las STP, and G6P6373/*C*Las STP, respectively, which reached equilibrium. The RMSF variances of the α-carbon residue of each residue in three complexes were calculated to find the flexibility of the protein structures. A higher RMSF value represents a much more flexible protein structure. Overall, the RMSF values of the three complexes ranged from 0.46 Å to 7.7 Å (Figure S3B). The outliers were from the tails. Although the N-terminal peptide covered the tails, they were still more flexible than the rest of the structure. No protein-ligand interactions were found at the last two amino acid positions, so the last two amino acids were excluded in subsequent RMSF analyses. After excluding these outliers, the RMSF ranged from 0.46 Å to 4.1 Å. Then, the average RMSF values were 1.33 Å, 1.32 Å, and 1.22 Å for G6P/*C*Las STP, G6P3510/*C*Las STP, and G6P6373/*C*Las STP, respectively. The two molecules screened, G6P3510 and G6P6373, caused lower RMSF values than G6P, indicating interactions between compounds and the protein (e.g., hydrogen bonding, hydrophobic interactions, ionic, and water bridge) had some impact on stabilizing the protein structure.

Intermolecular interaction analysis helps reveal the ligands' binding properties at the active site. For instance, in the G6P/*C*Las STP complex, the protein-ligand interaction diagram indicated the formation of three strong hydrogen bonds during a 100ns simulation (Figure S4A). The residues Lys 73, Lys 129, and Lys 67 formed hydrogen bonds with G6P, which lasted 110.5%, 62.1%, and 61.9% of the simulation time, respectively. A ratio greater than 100% indicates that a single residue simultaneously forms multiple hydrogen bonds with the ligand. Meanwhile, water bridge interactions were also detected on these three residues. In the last 1 ns frame of the simulation, G6P also formed three salt

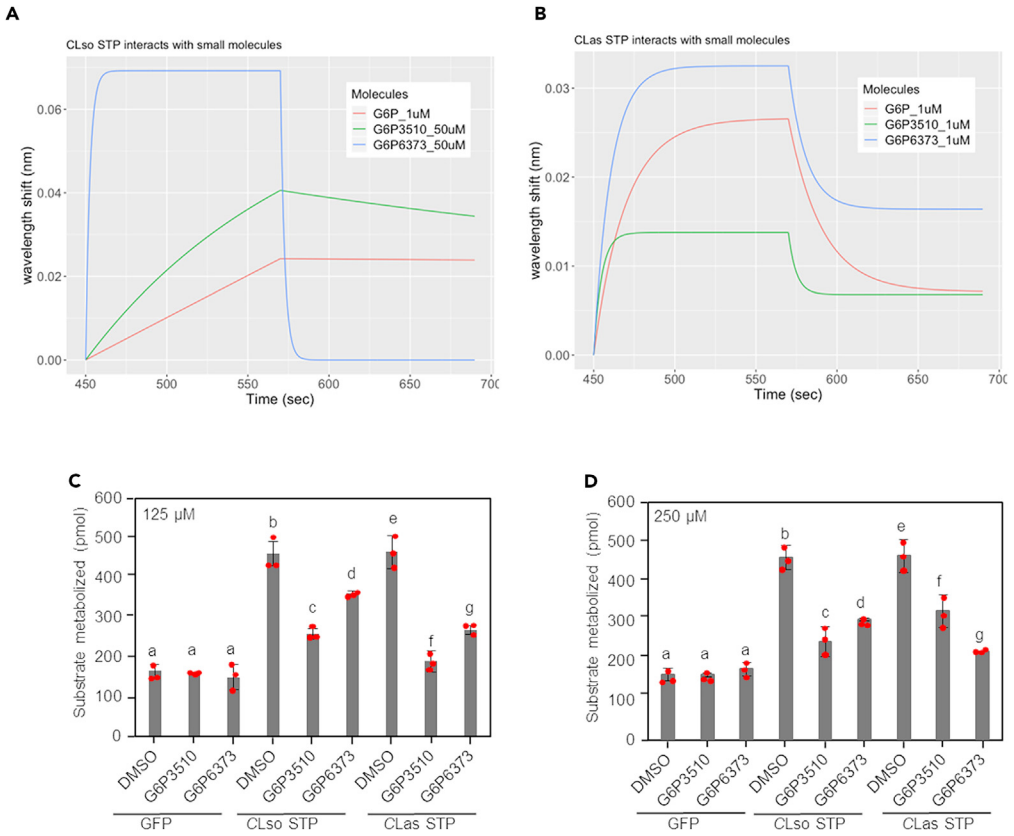

Figure 5. G6P3510 and G6P6373 bind to STP and inhibit phosphatase activity *in vitro*

The Biolayer interferometry (BLI) sensorgram shows the binding of *C*Lso STP (A) and CLas STP (B) with G6P3510 and G6P6373. Glucose-6-phosphate (G6P), a known phosphatase substrate, was used as a BLI assay reference control. All experiments were conducted in three replicates; each of the curves was globally fitted using three replicates. Phosphatase activity of *C*Lso and *C*Las STP in the presence of 125 μM (C) or 250 μM (D) of G6P3510 or G6P6373. Assays with GFP were used as a negative control. Statistically significant differences were determined by the Kruskal-Wallis test, followed by the Dunn's test for multiple pairwise comparisons. The p values were corrected for type I error using the Benjamini-Hochberg multiple testing correction. Different lowercase letters represent significant differences among the group means ($p \leq 0.05$). Data are represented as mean ± SEM.

bridges with the residue Lys 67 and Lys 73 at the active site, which increased the affinity for binding (Figure S5A). In the complex of G6P3510/*C*Las STP, multiple strong hydrogen bonds on residue Phe40, Thr41, Gln57, Asn 59, Lys 136, and Ser 137 were detected during the simulation, accounting for 71.9%, 124.8%, 15.1%, 2%, 72.2% and 20.6% of binding contribution during the MD simulation, respectively (Figures S4B and S5B). Due to the presence of an aromatic ring, strong hydrophobic interactions were detected at residues Phe 40, Ala 56, Tyr 169, Phe 172, and Pro 173, accounting for 8.1%, 7.6%, 14.9%, 46%, and 14.0%, respectively. Even though the small molecule remained in a fixed active site, stronger bonds were formed during the MD simulation. Also, the constant presence of hydrogen bonds indicated that the molecule bound stably at the active target site. In G6P6373/*C*Las STP complex, five central hydrogen bonds were detected at residue Gln 57 (32.6%), Gly 60 (28%), Lys 136 (70.4%), Thr 188 (21.2%), and Gln 189 (25.2%) (Figures S4C and S5C). Additionally, all these hydrogen bonds could switch to water-mediated ones during the simulation. Similar to the G6P3510 complex, this complex also detected more non-covalent bond formation during the simulation. All three molecules formed at least one or more stable non-covalent contacts with the protein throughout the simulations. In summary, the two screened compounds had better binding properties than G6P due to the observation of more protein-ligand contacts, and the simulation results confirmed the stability of the protein-ligand complexes.

G6P3510 and G6P6373 competitively bind to STP and inhibit phosphatase activity

To validate binding and determine the binding kinetics of the potential inhibitors of STPs, we performed ligand-binding assays using Bio-layer interferometry (BLI).[35] Briefly, recombinant *C*Lso and *C*Las STPs were produced in *Escherichia coli* with C-terminal 6xHis tag and purified by one-step purification using Ni column (Figure S6). Based on BLI binding kinetics data, the two test molecules, G6P3510 and G6P6373 along with the positive control G6P interacted on both STPs of CLso and CLas generating association and dissociation signals (Figures 5A and 5B; Table 2). For *C*Lso STP, the affinity constants, K_D, for G6P3510 and G6P6373 were 1.381×10^{-5} M and 1.42×10^{-2} M, respectively (Table 2). The K_D for the native substrate G6P was 6.688×10^{-6} M. The K_D values indicated that G6P3510 had an affinity closer to that of G6P (Table 2). A molecule with an affinity closer to but higher than the native substrate suggests competitive inhibition. Compared to G6P, G6P6373

Table 2. The kinetic energy analysis of the protein-ligand interactions

Ligand	Targeted protein	K_D (M)	K_a (1/Ms)	K_d (1/s)	R^2
G6P	*C*Lso STP	6.688×10^{-6}	1.758×10^{1}	1.176×10^{-4}	0.4832
G6P3510	*C*Lso STP	1.381×10^{-5}	1.064×10^{2}	1.469×10^{-3}	0.8156
G6P6373	*C*Lso STP	1.42×10^{-2}	2.691×10^{1}	3.82×10^{-1}	0.8876
G6P	*C*Las STP	2.361×10^{-5}	2.166×10^{3}	5.114×10^{-2}	0.7641
G6P3510	*C*Las STP	8.144×10^{-5}	1.285×10^{3}	1.047×10^{-1}	0.5428
G6P6373	*C*Las STP	2.401×10^{-5}	1.924×10^{3}	4.618×10^{-2}	0.6449

A known substrate, G6P was used as the positive control in this assay.

dissociated faster on CLso STP, leading to higher KD values and lower affinity. Compared to G6P, G6P3510 associated and dissociated faster; however, the compound's affinity was slightly lower than that of G6P. For *C*Las STP, the K_D for G6P3510 and G6P6373 was 8.144×10^{-5} M and 2.401×10^{-5} M, respectively, while it was 2.361×10^{-5} M for the native substrate G6P, indicating that both compounds had a comparable affinity to that of G6P (Table 2). It was evident that both the compounds had a comparable association rate to that of G6P; however, G6P3510 dissociated faster than the other two. Overall, the BLI kinetics data indicate that G6P6373 had a higher affinity to the active site than G6P3510, yet a lower affinity than the G6P native substrate, suggesting competitive inhibition.

Next, we tested if G6P3510 and G6P6373 can inhibit the STP phosphatase activity *in vitro*. For this, *C*Lso STP and *C*Las STP were expressed in *Arabidopsis* protoplasts as C-terminal HA-tag fusions and immunopurified using anti-HA beads. A GFP HA-tagged protein was simultaneously expressed and purified as a non-phosphatase control. The immunopurified STP and GFP proteins were treated with 125 μM or 250 μM G6P3510 (dissolved in 0.1% DMSO, along with mock (0.1% DMSO), followed by phosphatase assays. The results indicated that 125 μM and 250 μM G6P3510 and G6P6373 significantly inhibited *C*Las/*C*Lso STP phosphatase activity compared with the mock treatments (Figures 5C and 5D). Collectively, the results show that G6P3510 and G6P6373 can bind to and inhibit STP phosphatase activity *in vitro*.

G6P3510 and G6P6373 inhibit STP virulence function in planta

Since STP interfered with Prf^{D1416V}-mediated cell death[20,21] (Figure 2), we next tested if the G6P3510 and G6P6373 can block STP virulence function in planta. STP was co-infiltrated with Prf^{D1416V} in *N. benthamiana* (Figure 6). G6P3510 (50 μM, dissolved in 0.1% DMSO) or G6P6373 (50 μM, dissolved in 0.1% DMSO) were co-infiltrated with Prf^{D1416V} and CLas STP (Prf^{D1416V}+STP+G6P3510 or G6P6373), along with mock (DMSO 0.1%), Prf^{D1416V} alone, Prf^{D1416V} + STP, Prf^{D1416V} + EV, Prf^{D1416V} + EV + G6P3510 or G6P6373, and Prf^{D1416V} + G6P3510 or G6P6373. Leaves infiltrated with Prf^{D1416V} alone, Prf^{D1416V} + EV, and mock infiltrations served as controls. Five biological replicates were performed for each treatment (Figure 6). As expected, Prf^{D1416V}alone and EV infiltration resulted in the induction of prominent lesions by 15 dpi (Figure 6). In contrast, leaves co-infiltrated with Prf^{D1416V} + *C*Las or *C*Lso STP showed a significant reduction of lesions (Figure 6), similar to mock-infiltrated leaves (Figure 6). However, leaves co-infiltrated with G6P3510 or G6P6373 and Prf^{D1416V} + STP, the cell death lesions were strong and comparable to Prf^{D1416V} alone or other Prf^{D1416V} + EV controls (Figure 6). Collectively, these results support that G6P3510 and G6P6373 can inhibit STP activity in plant tissues.

G6P3510 and G6P6373 inhibit *Candidatus* Liberibacter spp. in plant tissues

Since STP interferes with plant immune responses (Figure 6) and is expressed in infected plant tissues (Figure 1), we next evaluated the effects of G6P3510 and G6P6373 on "*Candidatus* Liberibacter spp." accumulation. A major bottleneck to evaluating chemistries or therapies for "*Candidatus* Liberibacter spp." has been the fastidious or unculturable nature of the pathogens. Conventional assays rely on foliar sprays, stem injections, and grafting using whole plants, which can be inherently variable due to the challenges associated with the delivery of the inhibitors to the bacteria that reside unevenly within the mature plant vasculature.[36] We have recently demonstrated that plant hairy root matrices allow *ex vivo* propagation of "*Candidatus* Liberibacter spp." and can be used for faster antimicrobial assays and citrus genetic engineering.[37–39] Because hairy roots possess intact phloem and xylem that are anatomically and metabolically similar to normal plant vasculature,[40–42] they would also provide an *in planta* environment that is similar to the natural host environment for *C*Lso and *C*Las when compared to cell-free systems and using surrogate bacteria.[43–46]

The efficacy of the two potential inhibitors (G6P3510 and G6P6373) was first tested using the *C*Lso-potato and *C*Las-citrus hairy root cultures. Briefly, *C*Lso/*C*Las containing hairy roots were treated with G6P3510 and G6P6373 (5, 10, 20, and 50 μM, dissolved in 0.1% DMSO) for 72 h. Untreated and DMSO (0.1%) samples were used as controls. After treatment, all tissue samples were subjected to molecular diagnostics, and relative titers of the *C*Lso and *C*Las were estimated by qPCR analysis. Both G6P3510 and G6P6373 inhibited *C*Lso (FDR corrected $p \leq 0.01$) at all the dosages tested (5, 10, 20, and 50 μM) when compared to untreated controls (Figures 7C and 7D; Table S4). G6P3510 and G6P6373 also showed inhibitory activity against *C*Las at most tested dosages (FDR corrected $p \leq 0.05$ to 0.01) (Figures 7E and 7F; Table S5).

It is possible that G6P3510 and G6P6373 may inhibit unrelated plant- or other pathogen-encoded serine/tyrosine phosphatases. To investigate this, first, we performed BLASTP analysis of *C*Las/*C*Lso STPs and the predicted proteomes of potato, citrus, and *Pseudomonas*

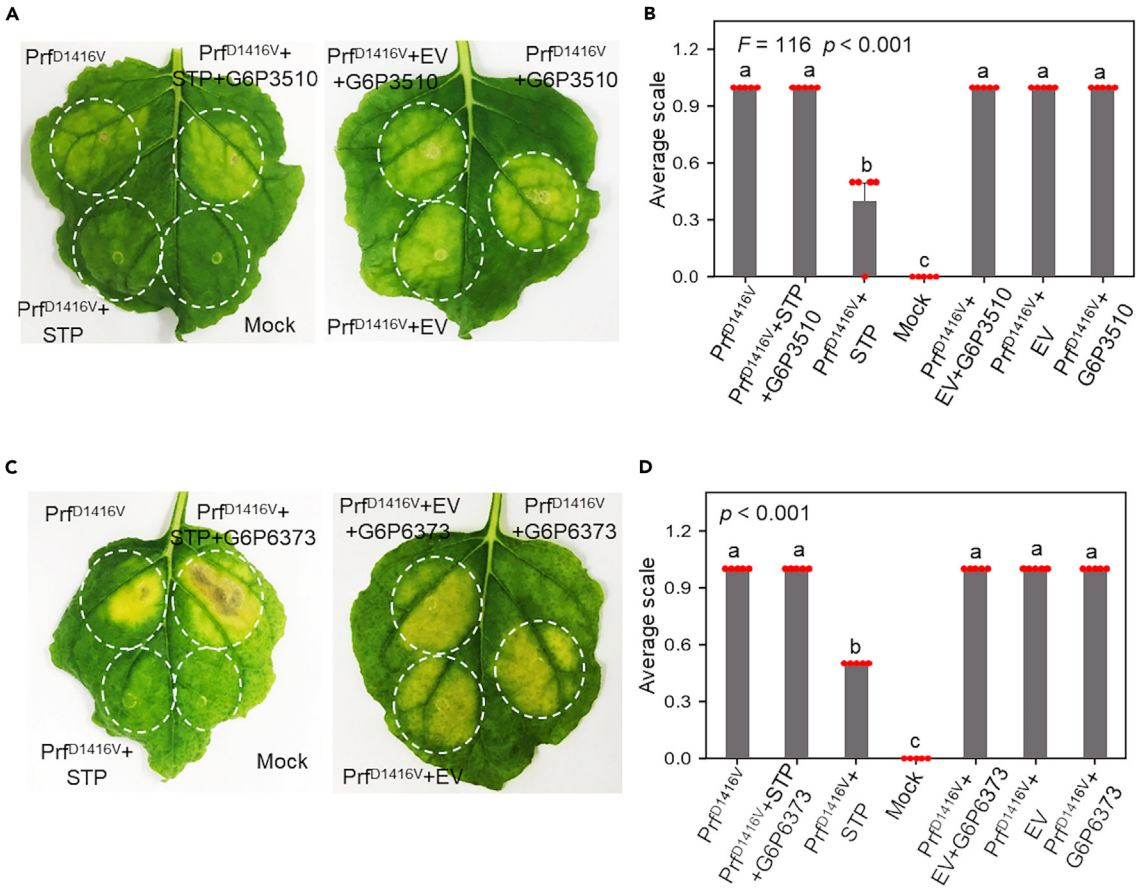

Figure 6. G6P3510 and G6P6373 inhibit STP activity in planta

A. tumefaciens co-infiltrations were performed by mixing 50 μM of G6P3510 (A and B) or G6P6373 (C and D) with Prf^{D1416V}, CLas STP (Prf^{D1416V}+STP+G6P3510 or G6P6373), along with mock (DMSO 0.1%), Prf^{D1416V} alone, Prf^{D1416V} + STP, Prf^{D1416V} + +empty vector (EV), Prf^{D1416V} + EV + G6P3510 or G6P6373, and Prf^{D1416V} + G6P3510 or G6P6373. Prf^{D1416V} induced cell lesions were assessed at 15 dpi. Representative images are shown in (A) and (C). Quantification of the data shown in (B) and (D) was done by scoring the cell lesion phenotypes of five independent biological replicates as follows: 0 = no lesions, 0.5 = moderate lesions, 1 = strong lesions. Data are represented as mean ± SEM (n = 5). Statistically significant differences were determined by one-way ANOVA followed by Tukey's HSD test. Different lowercase letters represent significant differences among the group means ($p \leq 0.05$). F and p values of ANOVA are indicated in (D). Data are represented as mean ± SE (n = 5). Statistically significant differences were determined by the Kruskal-Wallis test followed by the Dunn test for multiple pairwise comparisons. The p values were corrected for type I error using the Benjamini-Hochberg multiple testing correction. Different lowercase letters represent significant differences among the group means ($p \leq 0.05$). p values of the Kruskal-Wallis test are indicated in (D). Data are represented as mean ± SEM.

syringae. We did not find any significant matches to citrus proteins, while one significant (E-value <0.006) match was recovered in the potato (XP_006352385.1) and *P. syringae* (WP_052963584.1) proteomes. Both these matches, however, had poor coverage (~40–60%) and poor sequence conservation (~49–55% similarity) when compared to the high degree of conservation (>95% similarity) among the *Ca.* Liberibacter STPs (Figure 1A), suggesting that non-target effects on unrelated STPs are limited. Second, we tested the activity of G6P3510 and G6P6373 directly on *P. syringae* pv. *tomato* DC3000′ (*Pst*DC3000) growth *in vitro*. The results showed that neither of the molecules was inhibitory to *Pst*DC3000 growth (Figure S7), suggesting that non-target effects on unrelated microbes may be limited and underscoring the robustness of the target-based approach for finding specific inhibitors.

For preliminary proof of activity in planta, we focused on "*Candidatus* Liberibacter spp."-infected potato and citrus plants maintained in the greenhouse. The leaf tissues of these plants are generally amenable to penetration by either foliar spraying[37] or syringe infiltration.[47] For potato treatments, four-week-old plants were challenged with psyllids carrying *C*Lso, followed by foliar spraying G6P3510 and G6P6373 (10 and 50 μM, dissolved in 0.1% DMSO). The timeline, dosages, and frequency of applications were according to previously optimized methodologies.[37] Briefly, eight sprays were performed bi-weekly after the psyllid challenge. Chlorosis, wilting, and stunting disease symptoms on aerial shoots were monitored weekly, and qPCR-based molecular diagnostics were performed at 28 days post-infection (dpi). Characteristic symptoms of *C*Lso-infected potatoes, such as leaf curling and wilting, appeared in the control/untreated plants as early as 21 dpi and were exacerbated by 28 dpi (Figure 8A). Most plants died by 5–6 weeks. In contrast, the disease symptoms of plants treated with

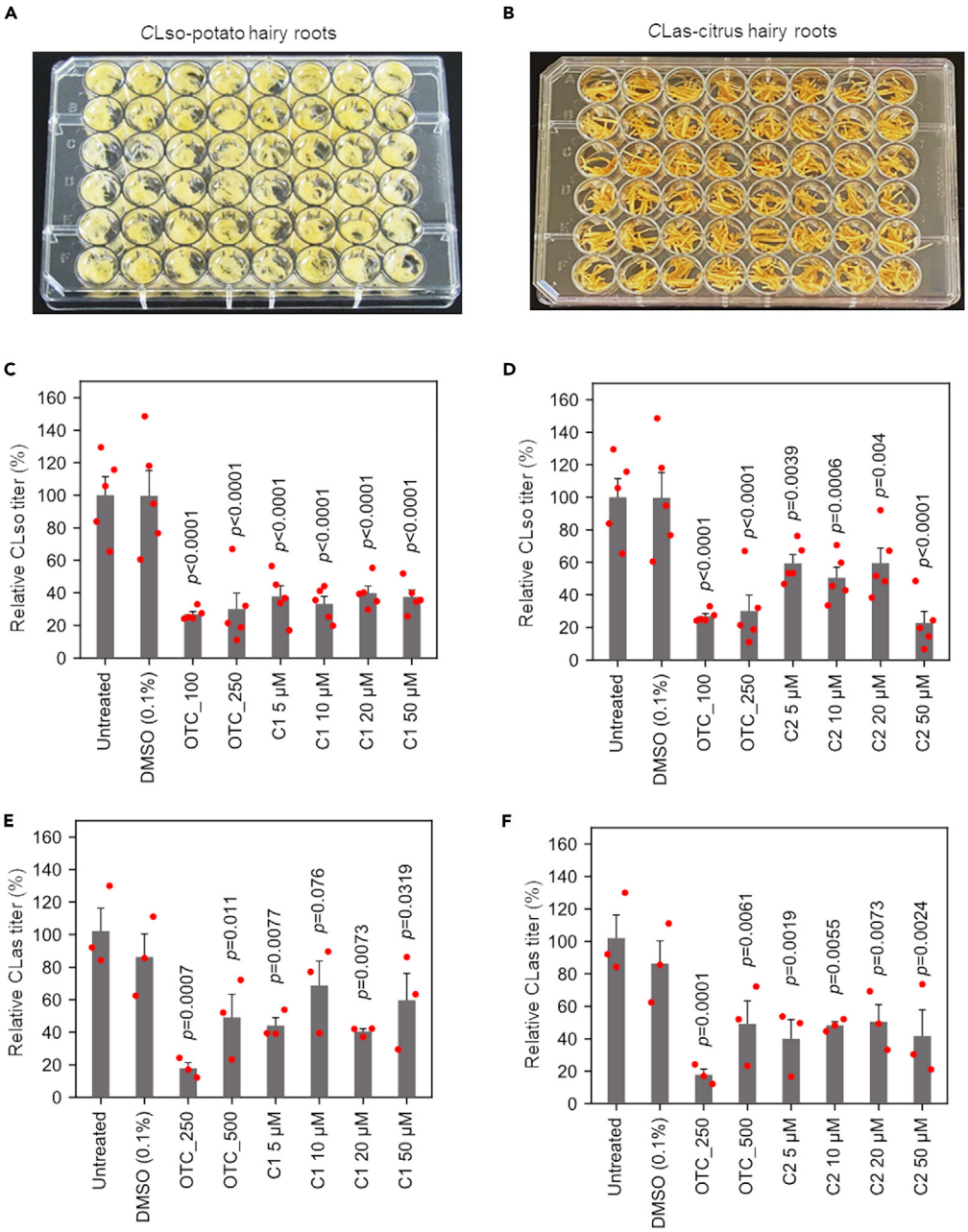

Figure 7. G6P3510 and G6P6373 inhibit '*Candidatus* Liberibacter spp.' in potato and citrus hairy root tissues

(A and B) Potato and citrus hairy roots (HR) infected with *C*Lso and *C*Las were treated with mock (DMSO) or 5, 10, 20, and 50 µM of G6P3510 (C1) and G6P6373 (C2) for 72 h. Relative titers of *C*Lso (C and D) and *C*Las (E and F) were estimated after 72 h of treatment by respective compounds, followed by qPCR analysis, along with untreated (UT) and DMSO (0.1%) treated samples. The bacterial titers were estimated relative to untreated samples set to 100%. Data are represented as mean ± SEM (n = 5 for [C and D] and n = 3 for [E and F]), and p values were estimated using one-way ANOVA followed by a post-hoc LSD test. The p values were corrected for multiple comparisons using the Benjamini-Hochberg (BH) FDR method. The experiment was independently repeated twice, and all replication attempts were successful.

G6P3510 and G6P6373 (10 and 50 µM, dissolved in 0.1% DMSO) were visually less prominent compared to the untreated controls at 28 dpi (Figures 8A and 8B). PCR diagnostics revealed a statistically significant (Tukey's HSD $p \leq 0.01$ to 0.005) decrease in *C*Lso accumulation in plants treated with G6P3510 and G6P6373 when compared to untreated controls (Figure 8C; Table S6), which correlated with the attenuated disease symptoms on the plants. Neither of the compounds exhibited phytotoxicity symptoms (e.g., chlorosis, necrosis, or stunting) on healthy plants throughout the developmental stages (Figure S8).

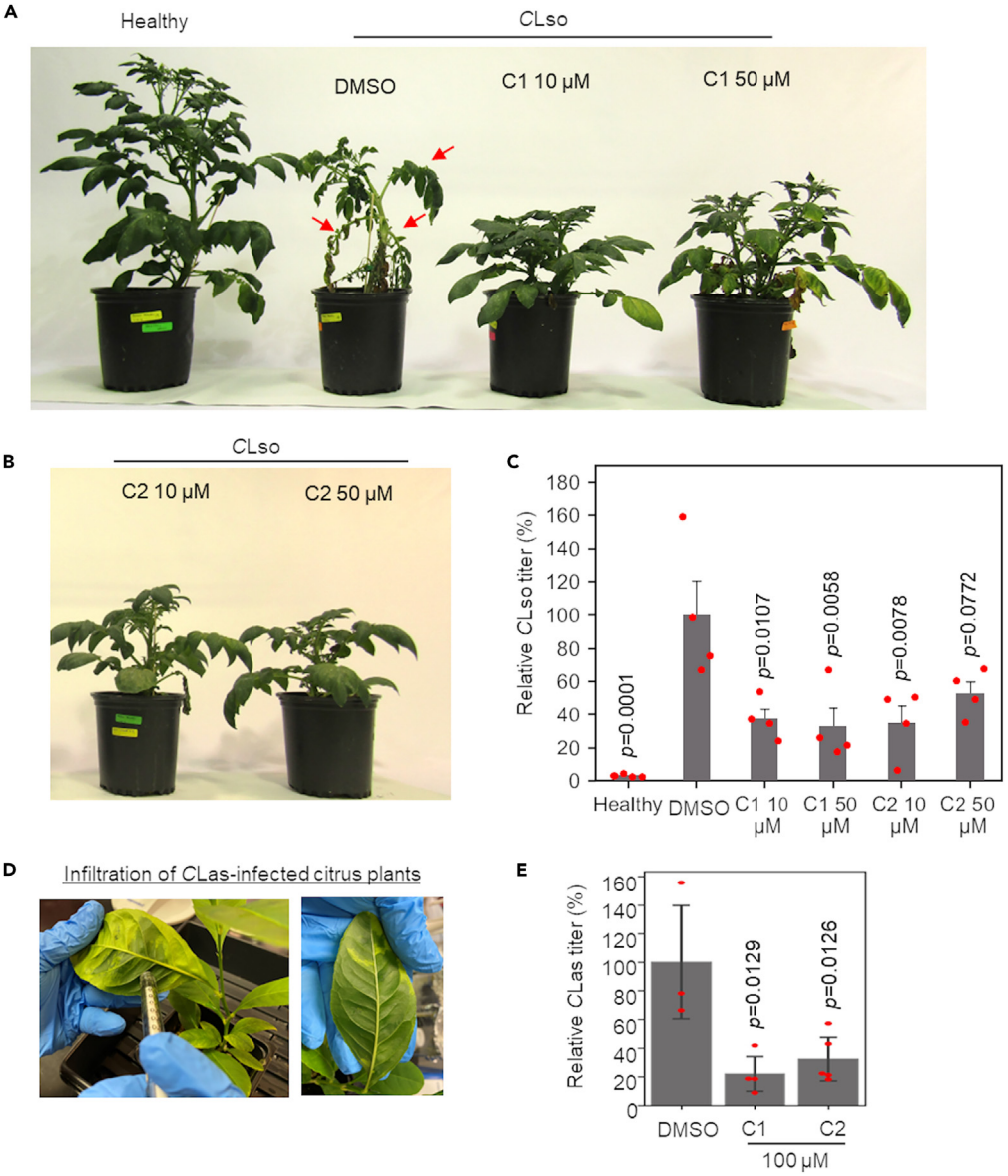

Figure 8. G6P3510 and G6P6373 cf. tolerance to "*Candidatus* Liberibacter spp."

(A and B) Visual symptoms of healthy and CLso-infected potato plants sprayed with mock (DMSO), 10 µM, and 50 µM solutions of G6P6373 (C1) and G6P3510 (C2). Red arrows indicate characteristic disease symptoms of CLso-infected potatoes, such as leaf curling and wilting.

(C) Relative titers of CLso in the mock, C1, and C2 treated plants at 28 days post-treatment.

(D) Leaves of CLas-infected citrus plants were infiltrated with mock (0.1% DMSO) or 100 µM solutions of G6P6373 (C1) and G6P3510 (C2).

(E) Relative titers of CLas in the mock, C1, and C2 treated plants at 28 days post-treatment. The relative bacterial titers were plotted relative to mock samples set to 100%. Data are represented as mean ± SEM (n = 3–5), and p values were estimated using one-way ANOVA followed by post hoc Tukey's HSD test.

For citrus in planta treatments, two fully expanded leaves of four to five-month-old CLas-positive citron rooted plants (n = 3 to 5 plants per treatment) were syringe-infiltrated[47] with a 0.1% DMSO (mock) solution or 100 µM solution of C1 and C2 (dissolved in 0.1% DMSO). The plants were subsequently maintained in the greenhouse, and leaves were sampled after 28 days to determine the relative CLas titers. The qPCR molecular diagnostics results showed significantly ($p \leq 0.01$) reduced CLas titers in C1 and C2 treated plants compared to mock plants (Figures 8D and 8E; Table S6). Combined with the hairy root bioassay results (Figure 7), the greenhouse plant trials sufficiently demonstrate the antimicrobial activity of the two molecules against *Candidatus* Liberibacter spp. in planta.

Limitations of the study

This study successfully employed an interdisciplinary approach of target-based molecular modeling and ligand screening to identify two pharmacophore-based inhibitors with demonstrated antimicrobial activity against "*Candidatus* Liberibacter spp." in hairy root assays and greenhouse plant experiments. Additional research would be needed to advance these antimicrobials as commercial products for practical application to manage HLB. For instance, unlike herbaceous crops like potatoes or greenhouse citrus plants, there are challenges associated with delivering active ingredients (AIs) into mature citrus trees in the field that are large, woody, and perennial. The waxy cuticle of the leaves is a barrier to the penetration of AIs by foliar application. Alternatively, trunk injections could deliver AIs into the citrus trees. However, only a few commercial products, mainly those based on oxytetracycline, were successfully delivered by trunk injections to manage HLB in citrus trees.[8]

In addition to possessing antimicrobial activity, the success of any new therapy in the field conditions is predicated on the physicochemical properties (e.g., solubility, pH, stability) of the AI that allow it to penetrate the plant cells and translocate systemically. In the current study, we used DMSO (0.1%), an EPA-approved inert ingredient (solvent or cosolvent) for pesticide formulations/products (https://www.federalregister.gov/d/2022-22129) to solubilize the AIs for foliar application and leaf infiltration studies. Further translocation and tracing studies in planta are needed to determine the systemicity of the new AIs. This will also aid in the selection of optimal carriers and formulation. Notably, multiple EPA-approved commercially available surfactants or carriers can be evaluated to enhance the absorption and subsequent translocation of AIs in planta.

Candidatus Liberibacter spp. accumulates considerably high levels in sink tissues such as young leaves and distal roots. Furthermore, in the case of HLB, citrus roots may act as a reservoir for CLas between periods of foliar flushing and seasonal fluctuations.[48,49] Hence, understanding the systemic movement and translocation of the AIs in planta can also help determine the impacts of the AIs on the bacterial communities in the root systems.

Another limitation to consider is the production scale and availability of the new AIs. Depending on the age and size of the citrus tree, the volume to treat could be much larger than the plants in the greenhouse, hence requiring significantly higher amounts of AIs. Because the new AIs are experimental compounds, the current synthesis scales are smaller (Table S7). The synthesis needs to be scaled up for large-scale field tree studies and applications to produce sufficient quantities. This will also help lower the costs of the interventions and make them profitable (Tables S7 and S8).

Lastly, as with any new AIs entering commercialization, they must undergo rigorous human and environmental safety assessments and obtain federal (e.g., EPA, FDA) regulatory approvals, likely in collaboration with the industry, before they can be safely deployed as commercial pest control products.

STAR★METHODS

Detailed methods are provided in the online version of this paper and include the following:

- KEY RESOURCES TABLE
- RESOURCE AVAILABILITY
  - Lead contact
  - Materials availability
  - Data and code availability
- EXPERIMENTAL MODEL AND STUDY PARTICIPANT DETAILS
  - Plant and insect propagation
- METHODS DETAIL
  - STP comparative genomics and phylogenetics and expression analysis
  - Homology modeling, pharmacophore identification, and ligand screening
  - Molecular dynamics simulation
  - STP expression, protoplast transfection, immunopurification, and phosphatase activity assays
  - Bio-layer interferometry (BLI) and binding kinetics assays
  - *In vitro* and *in planta* efficacy trials
  - DNA isolation and qPCR diagnostics
- QUANTIFICATION AND STATISTICAL ANALYSIS

SUPPLEMENTAL INFORMATION

Supplemental information can be found online at https://doi.org/10.1016/j.isci.2024.109232.

ACKNOWLEDGMENTS

The authors acknowledge Denise Rossi, Corrine Laughlin, Victoria Mora, and Michelle Dominguez (Texas A&M AgriLife Research, Weslaco, TX) for various technical support. This study was supported in part by funds from USDA-NIFA-ECDRE (2021-70029-36056, 2019-70016-29796; 2018-70016-28198; HATCH 1023984) to K.M., V.A., S.F., and G.C., and Texas A&M AgriLife Research Insect-Vectored Disease Seed grants

(124190-96210) and the Texas A&M AgriLife Institute for Advancing Health through agriculture to K.M.. We also acknowledge the support of Texas A&M High Performance Research Computing (HPRC) and the Laboratory for Molecular Simulation (LMS).

AUTHOR CONTRIBUTIONS

K.M., S.I., S.F., V.A., P.H., and G.C. designed the experiments and supervised the study. H.W., S.I., J.L., M.R., C.P., R.B., C.Y., S.T., and N.M. conducted the experiments and analyzed the data. H.W. and S.I. prepared the manuscript drafts. All authors reviewed and edited the manuscript.

DECLARATION OF INTERESTS

All authors declare no competing interests.

Received: October 3, 2023
Revised: November 8, 2023
Accepted: February 9, 2024
Published: February 15, 2024

REFERENCES

1. Greenway, G. (2014). Economic impact of zebra chip control costs on grower returns in seven US states. Am. Potato J. *91*, 714–719.
2. Hodges, A.W., and Spreen, T.H. (2012). Economic Impacts of Citrus Greening (HLB) in Florida, 2006/07–2010/111 (The Institute of Food and Agricultural Sciences).
3. Garnier, M., Jagoueix-Eveillard, S., Cronje, P.R., Le Roux, H.F., and Bové, J.M. (2000). Genomic characterization of a liberibacter present in an ornamental rutaceous tree, Calodendrum capense, in the Western Cape province of South Africa. Proposal of '*Candidatus* Liberibacter africanus subsp capensis'. Int. J. Syst. Evol. Microbiol. *50* (Pt 6), 2119–2125. https://doi.org/10.1099/00207713-50-6-2119.
4. Aubert, B., and Bové, J. (1980). Effect of penicillin or tetracycline injections of citrus trees affected by greening disease under field conditions in Réunion Island. In 8.
5. Martinez, A. (1975). Response of the etiologic agent of citrus greening disease in the Philippines to treatment with broad spectrum antibiotics. Philippine Phytopathol. *11*, 58–61.
6. Martinez, A., Nora, D., and Armedilla, A. (1970). Suppression of symptoms of citrus greening disease in the Philippines by treatment with tetracycline antibiotics. Plant Dis. Rep. *54*, 1007–1009.
7. Vincent, C.I., Hijaz, F., Pierre, M., and Killiny, N. (2022). Systemic Uptake of Oxytetracycline and Streptomycin in Huanglongbing-Affected Citrus Groves after Foliar Application and Trunk Injection. Antibiotics *11*, 1092.
8. Archer, L., Kunwar, S., Alferez, F., Batuman, O., and Albrecht, U. (2022). Trunk injection of oxytetracycline for huanglongbing management in mature grapefruit and sweet orange trees. Phytopathology *113*, 1010–1021.
9. National Academies of Sciences, E., and Medicine (2018). A Review of the Citrus Greening Research and Development Efforts Supported by the Citrus Research and Development Foundation: Fighting a Ravaging Disease (National Academies Press).
10. Kumar, K., Gupta, S.C., Chander, Y., and Singh, A.K. (2005). Antibiotic use in agriculture and its impact on the terrestrial environment. Adv. Agron. *87*, 1–54.
11. Editorial. (2019). Spraying diseased citrus orchards with antibiotics could backfire. Nature.
12. Serrano, M., Kombrink, E., and Meesters, C. (2015). Considerations for designing chemical screening strategies in plant biology. Front. Plant Sci. *6*, 131. https://doi.org/10.3389/fpls.2015.00131.
13. Zabotina, O., Malm, E., Drakakaki, G., Bulone, V., and Raikhel, N. (2008). Identification and preliminary characterization of a new chemical affecting glucosyltransferase activities involved in plant cell wall biosynthesis. Mol. Plant *1*, 977–989.
14. Yoshitani, N., Satou, K., Saito, K., Suzuki, S., Hatanaka, H., Seki, M., Shinozaki, K., Hirota, H., and Yokoyama, S. (2005). A structure-based strategy for discovery of small ligands binding to functionally unknown proteins: Combination of in silico screening and surface plasmon resonance measurements. Proteomics *5*, 1472–1480.
15. Cong, Q., Kinch, L.N., Kim, B.-H., and Grishin, N.V. (2012). Predictive Sequence Analysis of the Candidatus Liberibacter asiaticus Proteome. PLoS One *7*, e41071. https://doi.org/10.1371/journal.pone.0041071.
16. Wang, J., Haapalainen, M., Schott, T., Thompson, S.M., Smith, G.R., Nissinen, A.I., and Pirhonen, M. (2017). Genomic sequence of '*Candidatus* Liberibacter solanacearum' haplotype C and its comparison with haplotype A and B genomes. PLoS One *12*, e0171531.
17. Thapa, S.P., De Francesco, A., Trinh, J., Gurung, F.B., Pang, Z., Vidalakis, G., Wang, N., Ancona, V., Ma, W., and Coaker, G. (2020). Genome-wide analyses of Liberibacter species provides insights into evolution, phylogenetic relationships, and virulence factors. Mol. Plant Pathol. *21*, 716–731. https://doi.org/10.1111/mpp.12925.
18. Lorenz, U. (2011). Protein tyrosine phosphatase assays. Curr. Protoc. Im. *93*, 11.7.
19. Jeffrey, K.L., Camps, M., Rommel, C., and Mackay, C.R. (2007). Targeting dual-specificity phosphatases: manipulating MAP kinase signalling and immune responses. Nat. Rev. Drug Discov. *6*, 391–403.
20. Levy, J.G., Gross, R., Mendoza-Herrera, A., Tang, X., Babilonia, K., Shan, L., Kuhl, J.C., Dibble, M.S., Xiao, F., and Tamborindeguy, C. (2020). Lso-HPE1, an Effector of 'Candidatus Liberibacter solanacearum', Can Repress Plant Immune Response. Phytopathology *110*, 648–655.
21. Du, X., Miao, M., Ma, X., Liu, Y., Kuhl, J.C., Martin, G.B., and Xiao, F. (2012). Plant programmed cell death caused by an autoactive form of Prf is suppressed by co-expression of the Prf LRR domain. Mol. Plant *5*, 1058–1067.
22. Berman, H.M., Westbrook, J., Feng, Z., Gilliland, G., Bhat, T.N., Weissig, H., Shindyalov, I.N., and Bourne, P.E. (2000). The Protein Data Bank. Nucleic Acids Res. *28*, 235–242. https://doi.org/10.1093/nar/28.1.235.
23. Raththagala, M., Brewer, M.K., Parker, M.W., Sherwood, A.R., Wong, B.K., Hsu, S., Bridges, T.M., Paasch, B.C., Hellman, L.M., Husodo, S., et al. (2015). Structural Mechanism of Laforin Function in Glycogen Dephosphorylation and Lafora Disease. Mol. Cell *57*, 261–272. https://doi.org/10.1016/j.molcel.2014.11.020.
24. Remmert, M., Biegert, A., Hauser, A., and Söding, J. (2011). HHblits: lightning-fast iterative protein sequence searching by HMM-HMM alignment. Nat. Methods *9*, 173–175. https://doi.org/10.1038/Nmeth.1818.
25. Humphrey, W., Dalke, A., and Schulten, K. (1996). VMD: Visual molecular dynamics. J. Mol. Graph. *14*, 33. https://doi.org/10.1016/0263-7855(96)00018-5.
26. Trott, O., and Olson, A.J. (2010). Software news and update AutoDock Vina: Improving the speed and accuracy of docking with a new scoring function, efficient optimization, and multithreading. J. Comput. Chem. *31*, 455–461. https://doi.org/10.1002/jcc.21334.
27. Phillips, J.C., Braun, R., Wang, W., Gumbart, J., Tajkhorshid, E., Villa, E., Chipot, C., Skeel, R.D., Kalé, L., and Schulten, K. (2005). Scalable molecular dynamics with NAMD. J. Comput. Chem. *26*, 1781–1802. https://doi.org/10.1002/jcc.20289.
28. Bakan, A., Nevins, N., Lakdawala, A.S., and Bahar, I. (2012). Druggability assessment of allosteric proteins by dynamics simulations in the presence of probe molecules. J. Chem. Theor. Comput. *8*, 2435–2447. https://doi.org/10.1021/ct300117j.

29. Fernando, S., and Fernando, T. (2017). Antivirals for allosteric inhibition of Zika virus using a homology model and experimentally determined structure of envelope protein. BMC Res. Notes *10*, 354.
30. Fernando, S., Fernando, T., Stefanik, M., Eyer, L., and Ruzek, D. (2016). An approach for Zika virus inhibition using homology structure of the envelope protein. Mol. Biotechnol. *58*, 801–806.
31. Wang, H., Mulgaonkar, N., Pérez, L.M., and Fernando, S. (2022). ELIXIR-A: An Interactive Visualization Tool for Multi-Target Pharmacophore Refinement. ACS Omega *7*, 12707–12715.
32. Koes, D.R., and Camacho, C.J. (2012). ZINCPharmer: pharmacophore search of the ZINC database. Nucleic Acids Res. *40*, W409–W414. https://doi.org/10.1093/nar/gks378.
33. Lipinski, C.A. (2004). Lead- and drug-like compounds: the rule-of-five revolution. Drug Discov. Today Technol. *1*, 337–341. https://doi.org/10.1016/j.ddtec.2004.11.007.
34. Lipinski, C.A. (2004). Lead-and drug-like compounds: the rule-of-five revolution. Drug Discov. Today Technol. *1*, 337–341.
35. Shah, N.B., and Duncan, T.M. (2014). Bio-layer interferometry for measuring kinetics of protein-protein interactions and allosteric ligand effects. J. Vis. Exp. e51383.
36. Li, J., Pang, Z., Duan, S., Lee, D., Kolbasov, V.G., and Wang, N. (2019). The in planta effective concentration of oxytetracycline against *Candidatus* Liberibacter asiaticus for suppression of citrus Huanglongbing. Phytopathology *109*, 2046–2054.
37. Irigoyen, S., Ramasamy, M., Pant, S., Niraula, P., Bedre, R., Gurung, M., Rossi, D., Laughlin, C., Gorman, Z., Achor, D., et al. (2020). Plant hairy roots enable high throughput identification of antimicrobials against *Candidatus* Liberibacter spp. Nat. Commun. *11*, 5802. https://doi.org/10.1038/s41467-020-19631-x.
38. Kennedy, J.P., Wood, K., Pitino, M., Mandadi, K., Igwe, D.O., Shatters, R.G., Jr., Widmer, T.L., Niedz, R., and Heck, M. (2023). A perspective on current therapeutic molecule screening methods against 'Candidatus Liberibacter asiaticus', the presumed causative agent of citrus Huanglongbing. Phytopathology *113*, 1171–1179.
39. Ramasamy, M., Dominguez, M.M., Irigoyen, S., Padilla, C.S., and Mandadi, K.K. (2023). *Rhizobium rhizogenes*-mediated hairy root induction and plant regeneration for bioengineering citrus. Plant Biotechnol. J. *21*, 1728–1730.
40. Ron, M., Dorrity, M.W., de Lucas, M., Toal, T., Hernandez, R.I., Little, S.A., Maloof, J.N., Kliebenstein, D.J., and Brady, S.M. (2013). Identification of novel loci regulating interspecific variation in root morphology and cellular development in tomato. Plant Physiol. *162*, 755–768. https://doi.org/10.1104/pp.113.217802.
41. Lucas, M., Swarup, R., Paponov, I.A., Swarup, K., Casimiro, I., Lake, D., Peret, B., Zappala, S., Mairhofer, S., Whitworth, M., et al. (2011). SHORT-ROOT regulates primary, lateral, and adventitious root development in *Arabidopsis*. Plant Physiol. *155*, 384–398. https://doi.org/10.1104/pp.110.165126.
42. Ron, M., Kajala, K., Pauluzzi, G., Wang, D., Reynoso, M.A., Zumstein, K., Garcha, J., Winte, S., Masson, H., Inagaki, S., et al. (2014). Hairy root transformation using *Agrobacterium rhizogenes* as a tool for exploring cell type-specific gene expression and function using tomato as a model. Plant Physiol. *166*, 455–469. https://doi.org/10.1104/pp.114.239392.
43. Davis, M.J., Mondal, S.N., Chen, H., Rogers, M.E., and Brlansky, R.H. (2008). Co-cultivation of '*Candidatus* Liberibacter asiaticus' with Actinobacteria from Citrus with Huanglongbing. Plant Dis. *92*, 1547–1550. https://doi.org/10.1094/PDIS-92-11-1547.
44. Leonard, M.T., Fagen, J.R., Davis-Richardson, A.G., Davis, M.J., and Triplett, E.W. (2012). Complete genome sequence of Liberibacter crescens BT-1. Stand. Genomic Sci. *7*, 271–283.
45. Barnett, M.J., Solow-Cordero, D.E., and Long, S.R. (2019). A high-throughput system to identify inhibitors of *Candidatus* Liberibacter asiaticus transcription regulators. Proc. Natl. Acad. Sci. USA *116*, 18009–18014.
46. Jain, M., Cai, L., Fleites, L.A., Munoz Bodnar, A., Davis, M.J., and Gabriel, D.W. (2019). Liberibacter crescens is a cultured surrogate for functional genomics of uncultured pathogenic '*Candidatus* Liberibacter'spp. and is naturally competent for transformation. Phytopathology *109*, 1811–1819.
47. Francis, M.I., Kostenyuk, I., Orbović, V., Loskutov, A., Zolotukhin, M., and Graham, J.H. (2011). Automated needle-free injection method for delivery of bacterial suspensions into citrus leaf tissues. J. Phytopathol. *159*, 347–351.
48. Johnson, E.G., Wu, J., Bright, D.B., and Graham, J.H. (2014). Association of '*Candidatus* Liberibacter asiaticus' root infection, but not phloem plugging with root loss on huanglongbing-affected trees prior to appearance of foliar symptoms. Plant Pathol. *63*, 290–298.
49. Sauer, A.V., Zanutto, C.A., Nocchi, P.T.R., Machado, M.A., Bock, C.H., and Nunes, W.M.C. (2015). Seasonal variation in populations of '*Candidatus* Liberibacter asiaticus' in citrus trees in Paraná state, Brazil. Plant Dis. *99*, 1125–1132.
50. Sengoda, V.G., Cooper, W.R., Swisher, K.D., Henne, D.C., and Munyaneza, J.E. (2014). Latent period and transmission of "*Candidatus* Liberibacter solanacearum" by the potato psyllid *Bactericera cockerelli* (Hemiptera: Triozidae). PLoS One *9*, e93475. https://doi.org/10.1371/journal.pone.0093475.
51. Lin, H., Islam, M.S., Bai, Y., Wen, A., Lan, S., Gudmestad, N.C., and Civerolo, E.L. (2012). Genetic diversity of '*Cadidatus* Liberibacter solanacearum'strains in the United States and Mexico revealed by simple sequence repeat markers. Eur. J. Plant Pathol. *132*, 297–308.
52. Löytynoja, A. (2014). Phylogeny-aware alignment with PRANK. In Multiple sequence alignment methods (Springer), pp. 155–170.
53. Stamatakis, A. (2006). RAxML-VI-HPC: maximum likelihood-based phylogenetic analyses with thousands of taxa and mixed models. Bioinformatics *22*, 2688–2690.
54. Rambaut, A., and Drummond, A. (2012). FigTree version 1.4. 0.
55. Release, S. (2017). 4: Desmond Molecular Dynamics System (DE Shaw Research).
56. Wizard, P.P. (2014). Epik version 2.8 (Schrödinger, LLC).
57. Release, S. (2017). 1: Maestro (Schrödinger, LLC).
58. Release, S. (2018). 4: Glide (Schrödinger, LLC).
59. Roos, K., Wu, C., Damm, W., Reboul, M., Stevenson, J.M., Lu, C., Dahlgren, M.K., Mondal, S., Chen, W., Wang, L., et al. (2019). OPLS3e: Extending Force Field Coverage for Drug-Like Small Molecules. J. Chem. Theor. Comput. *15*, 1863–1874. https://doi.org/10.1021/acs.jctc.8b01026.
60. Ciesielski, G.L., Hytonen, V.P., and Kaguni, L.S. (2016). Biolayer interferometry: A novel method to elucidate protein-protein and protein-DNA interactions in the mitochondrial DNA replisome. In Methods Mol Biol, M. McKenzie, ed., pp. 223–231. https://doi.org/10.1007/978-1-4939-3040-1_17.
61. Levy, J., Ravindran, A., Gross, D., Tamborindeguy, C., and Pierson, E. (2011). Translocation of '*Candidatus* Liberibacter solanacearum', the Zebra Chip Pathogen, in Potato and Tomato. Phytopathology *101*, 1285–1291. https://doi.org/10.1094/PHYTO-04-11-0121.
62. Zheng, Z., Xu, M., Bao, M., Wu, F., Chen, J., and Deng, X. (2016). Unusual five copies and dual forms of nrdB in "*Candidatus* Liberibacter asiaticus": Biological implications and PCR detection application. Sci. Rep. *6*, 39020.
63. Livak, K.J., and Schmittgen, T.D. (2001). Analysis of relative gene expression data using real-time quantitative PCR and the $2^{-\Delta\Delta CT}$ method. Methods *25*, 402–408.
64. Benjamini, Y., and Hochberg, Y. (1995). Controlling the false discovery rate- a practical and powerful approach to multiple testing. J. Roy. Stat. Soc. B *57*, 289–300.
65. Almeyda León, I.H., Rocha Peña, M.A., Piña Razo, J., and Martínez Soriano, J.P. (2001). The use of polymerase chain reaction and molecular hybridization for detection of phytoplasmas in different plant species in México. Rev. Mex. Fitopatol. *19*, 1–9.

STAR★METHODS

KEY RESOURCES TABLE

REAGENT or RESOURCE	SOURCE	IDENTIFIER
Antibodies		
Anti-HA peroxidase monoclonal antibody	Roche	Cat# 12013819001; RRID: AB_390917
Mouse Anti-His monoclonal antibody	Genscript	Cat# A00186
Bacterial and virus strains		
Candidatus Liberibacter spp.	This study	N/A
Chemicals, peptides, and recombinant proteins		
CLso STP recombinant protein	This study	N/A
CLas STP recombinant protein	This study	N/A
G6P3510 chemical	This study	MCULE ID-8749857699-0
G6P6373 chemical	This study	MCULE ID-4680703503
Experimental models: Organisms/strains		
Solanum tuberosum L. var. Atlantic	This study	N/A
Bactericera cockerelli (Šulc)	This study	N/A
Oligonucleotides		
Primers used for qPCR and RT-qPCR	This study	Table S2
Recombinant DNA		
pHBT-binary vector containing CLas or CLso STP-HA	This study	N/A
PrfD1416V plasmid	Du et al., 2012	N/A
Software and algorithms		
ELIXIR-A	GitHub	https://github.com/sfernando-BAEN/ELIXIR-A
	GitHub	https://github.com/sfernando-BAEN/ELIXIR-A-Vina-Batch-Screening-Module
Bioinfokit	GitHub	https://github.com/mandadi-lab/bioinfokit
Other		
Genbank accession numbers for '*Candidatus* Liberibacter spp.' STP proteins.	This study	Table S1
BLItz/Octet N1 system with Anti-Penta-HIS (HIS1K) Biosensors	Sartorius	https://www.sartorius.com/en/products/protein-analysis/octet-bli-detection/octet-label-free-detection-systems/octet-n1

RESOURCE AVAILABILITY

Lead contact

Further information and requests for resources and reagents should be directed to and will be fulfilled by the lead contact, Kranthi Mandadi (kkmandadi@tamu.edu).

Materials availability

There are restrictions on the availability of some materials due to the limited amount of the original stocks and/or quarantines associated with regulated pathogens. Direct inquiries regarding the materials generated as part of this study should be directed to the lead contact, Kranthi Mandadi (kkmandadi@tamu.edu).

Data and code availability

- All data is made available in the manuscript and related supplementary files. Accession numbers are listed in the supplementary tables and key resources table. The Python bioinfokit package used for data analysis and visualization was deposited on GitHub [https://github.com/mandadi-lab/bioinfokit].
- The source code for algorithms used for pharmacophore mapping was deposited in GitHub [https://github.com/sfernando-BAEN/ELIXIR-A] and [https://github.com/sfernando-BAEN/ELIXIR-A-Vina-Batch-Screening-Module]. All code is publicly available and was last accessed on 29 Jan 2024.
- Any additional information required to reanalyze the data reported in this paper is available from the lead contact upon request.

EXPERIMENTAL MODEL AND STUDY PARTICIPANT DETAILS

Plant and insect propagation

Potato (*Solanum tuberosum* L. var. Atlantic) plants were grown in Metro-Mix® 360 (Sungro Horticulture, MA, USA) in a growth chamber under the following conditions: 21-22°C, a 14-h/10-h light/dark photoperiod, and 50% relative humidity. *Bactericera cockerelli* (Šulc) psyllids, both *C*Lso-positive (haplotype B) and *C*Lso-negative, were collected in the Rio Grande Valley in Texas,[50] and maintained in the laboratory in nylon cages (Bugdorm, Taiwan). The presence and haplotype of '*Candidatus* Liberibacter solanacearum' (*C*Lso) in psyllid colonies were periodically confirmed by PCR using primers specific for the single sequence repeat (SSR) loci of *C*Lso (SSR-F and SSR-R, Table S2).[51]

METHODS DETAIL

STP comparative genomics and phylogenetics and expression analysis

C. Liberibacter spp. STP sequences and NCBI accession numbers used for multiple sequence alignment and phylogenetic analyses are provided in Table S1. Multiple alignments of protein sequences were performed with prank PRANK v.170427.[52] Phylogenetic analyses were performed using a maximum likelihood approach in RAxML 8.2 with 1,000 bootstrap replicates.[53] The resulting phylogeny was visualized using FigTree 1.4.3.[54] Expression of STP in *C*Lso- and *C*Las-infected potato and citrus tissues was confirmed using reverse-transcription (RT)-PCR. Briefly, total plant RNA was isolated from 50 mg of symptomatic leaf tissue using the Direct-zol RNA Miniprep kit (Zymo Research, Irvine, CA), following the manufacturer's instructions. The RNA quality and concentration were evaluated by gel electrophoresis and NanoDrop1000 spectrophotometer, respectively (Thermo Fisher Scientific, Waltham, MA). One μg of RNA was used to prepare complementary DNA using Invitrogen Superscript IV Reverse Transcriptase following the manufacturer's instructions (Thermo Fisher Scientific, Waltham, MA), followed by PCR amplification using STP gene-specific primers (Table S2).

Homology modeling, pharmacophore identification, and ligand screening

The inhibitor screening was performed in several steps, beginning with developing the STP homology model, identifying active sites and pharmacophores, and then ligand/inhibitor screening. Simulation platforms, including Autodock Vina,[26] Visual Molecular Dynamics (VMD),[25] Drugui,[28] Enhanced Ligand Exploration and Interaction Recognition Algorithm (ELIXIR-A),[29–31] Nanoscale Molecular Dynamics (NAMD)[27] were used during *in silico* analysis. ELIXIR-A, the algorithm created for pharmacophore mapping, was deposited in GitHub [https://github.com/sfernando-BAEN/ELIXIR-A] and [https://github.com/sfernando-BAEN/ELIXIR-A-Vina-Batch-Screening-Module]. NAMD simulations were performed in the Texas A&M High Performance Research Computing. To perform MD simulations using NAMD, four separate files were used: A Protein Data Bank (PDB or .pdb) file that stores atomic coordinates and velocities for the system; A Protein Structure File (PSF or .psf) that holds structural information of the protein, such as various types of bonding interactions; A force field parameter file that contains the mathematical expressions of the potentials experienced by the atoms in the system; and a configuration file in which the user specifies all the options that NAMD should use in running a simulation. These files were created by substrate ligands and probe molecules (small molecule alcohols, amines, amides, and esters) that were used to interrogate the enzymes' active sites. Small probes were selected so they could diffuse rapidly and explore small and even transient pockets in the simulations. This property also helps sample many binding events while enabling equilibrium in reasonable timeframes. The binding hotspots (pharmacophores) were isolated by selecting high-affinity probe binding spots, clustering them, and merging them to assess high-affinity sites.[28] All the interaction diagrams were developed using Schrodinger Maestro software. ELIXIR-A[29–31] and the zincpharmer algorithm were used to screen and match the identified pharmacophores with potential inhibitors.[32] The top hits were selected based on the following criteria: i) a combination of the location of the functional groups (e.g., proton donor/acceptor, hydrophobic groups, positive/negative ion, and exclusion spheres); ii) stabilization of the most effective conformation; iii) Lipinski's rule of five that defines properties necessary for good permeation[34] (i.e., the molecule having less than five proton-donators, the molecular weight is less than 500 Daltons, log P smaller than 5, the molecule having < 10 acceptors, and the molecule using biological transporters so that the ligand does not attach too strong); iv) Molinspiration drug-likeness & bioactivity score (www.molinspiration.com), and v) having at least three pharmacophoric points.

Molecular dynamics simulation

A 100 ns MD simulation was performed using the Schrödinger-Desmond platform to analyze STP proteins' conformational and interaction stability in complex with screened ligands.[55] The *C*Las STP protein was prepared by Maestro's Protein Preparation Wizard.[56,57] C and N

termini were capped to reduce the flexibility of the termini. For the screened ligands, Schrödinger's Glide extra-precision mode was used to reproduce the docking poses from the previous Vina docking studies.[58] The ligand-protein complexes were minimized under the OPLS3e force field.[59] The system was solvated using an SPC solvent model with orthogonal boundary conditions maintaining a buffer distance of 5 Å. The system charge was neutralized using chloride or sodium ions. Each system was minimized under the OPLS3e force field using Desmond's default relaxation protocol. The system was simulated under isothermal–isobaric conditions at 300 K and 1.01325 bar pressure. A thousand frames were recorded at every 100 ps following the initial frame. The Simulation Interaction Diagram (SID) module was used to assess the quality of the entire simulation over time, including protein-ligand interactions, complex root means square deviations (RMSD), and complex root means square fluctuations (RMSF).

STP expression, protoplast transfection, immunopurification, and phosphatase activity assays

The endogenous expression of STP in *C*Lso and *C*Las infected plant tissues (potato and citrus) was confirmed by Reverse Transcription Polymerase Chain Reaction (RT-PCR) analysis. Briefly, total RNA was extracted from healthy or infected shoot tissues (50 mg) using a Direct-zol RNA Miniprep kit (Zymo Research, Irvine, CA), following the manufacturer's instructions. The RNA concentration, integrity, and quality were checked using agarose gel electrophoresis and NanoDrop1000 spectrophotometer (Thermo Fisher Scientific, Waltham, MA). Using a random hexamer primer, one microgram of total RNA was converted to complementary DNA (cDNA) using a Superscript IV first-strand cDNA synthesis kit (Invitrogen). The cDNA was subsequently used for PCR amplification using *C*Lso and *C*Las STP-specific primers (Table S2).

For STP expression in Arabidopsis protoplasts and immuno-purification, the pHBT-binary vector-based *C*Las/*C*Lso STP-HA tagged constructs were made and used for transfection. Briefly, the Arabidopsis leaf strips were excised from the 4-week-old plants. They were lysed in an enzyme solution (1% cellulase R10, 0.2% macerozyme R10, 0.4 M mannitol, 20 mM KCl, 20 mM MES pH 5.7) at room temperature for 3-4 hours. The protoplasts were re-suspended in 0.5 mL W5 (154 mM NaCl, 125 mM $CaCl_2$, 5 mM KCl, 2 mM MES pH 5.7) solution by gentle shaking. Before PEG-Ca^{2+} transfection, the W5 protoplast solution was resuspended in MMg solution (0.4 M mannitol, 15 mM $MgCl_2$, 4 mM MES pH 5.7) at a density of 5 x 10^5-5 x 10^7 cells /mL. This density of protoplasts provided an excellent range to achieve measurable phosphatase activity. Next, 40% (w/v) PEG solution with 0.2 M mannitol and 100 mM $CaCl_2$ was used for PEG-Ca^{2+} transfection. After transfection, the protoplasts were resuspended in 50 µL WI (0.5 M mannitol, 20 mM KCl, 4 mM MES pH 5.7). Lastly, protoplasts were aliquoted into two wells of a 24-well tissue culture plate with 250 µL WI, and proteins were allowed to express by overnight incubation at room temperature. For immunopurification, the protoplasts were lysed by vertexing in an extraction buffer (100 mM NaCl, 1 mM EDTA, 20 mM Tris-HCl, pH 7.5, 2 mM NaF, 2 mM Na_3VO_4, 1 mM dithiothreitol (DTT), 0.5% Triton X-100, 10% glycerol and 1×protease inhibitor). After centrifugation at 14,000 g at 4°C for 20 min, 250 µL of extraction buffer was added to resuspend the pellet and incubated with anti-HA affinity beads (Sigma) at 4°C for 2h with gentle shaking. Beads were collected and washed three times with washing buffer (20 mM Tris-HCl, pH7.5, 100 mM NaCl, 1 mM EDTA, 1% Triton X-100) and once with 50 mM Tris-HCl, pH7.5. The beads were then resuspended in 100 µL 1 X phosphatase assay buffer (25 mM HEPES, pH 7.5, 0.2 mM EDTA, 10 mM DTT, 200 µg/mL BSA), and stored on ice until initiation of the phosphatase assay. An aliquot of the immunoprecipitated protein beads was analyzed by SDS-PAGE and immunoblotting with anti-HA peroxidase antibodies (Roche) to confirm the presence of the proteins before the phosphatase activity assays.

The CLso/CLas STP phosphatase activity was measured using p-Nitrophenyl Phosphate (pNPP) chromogenic substrate. In this assay, dephosphorylation of pNPP can be measured at absorbance (OD) 405 nm and used to calculate the enzymatic activity of the phosphatase. Briefly, 10 µL pNPP (Thermofisher, 250 mM in 1 x phosphatase assay buffer) was mixed with 40 µL immunoprecipitated STP protein beads in 1 x phosphatase assay buffer and incubated at 30°C for 30-45 minutes. The reaction was stopped by adding 1 mL of 1 N NaOH, and absorbance (OD) was read at 405 nm using the microplate reader (Agilent BioTek Cytation 7 Multimode Reader by Agilent Technologies). The enzyme activity was estimated using the following formula:

Enzyme activity [µmoles/min µg] = 50 [vol] x OD405 x 1/time [min] x enzyme [µg] x 1/ 18,000 [molar extinction coefficient].

G6P3510 and G6P6373 molecules were custom synthesized and purchased from Mcule. Chemical specifications (Formula, InChIKey, Smiles) and Mcule IDs of G6P3510 and G6P6373 are provided in Table S7. Next, the effects of G6P3510 and G6P6373 on CLso/CLas phosphatase activity were determined by pre-treating immunopurified proteins with G6P3510 and G6P6373 (125 µM or 250 µM, along with DMSO as mock, for around 15-30 min followed by addition of the pNPP to start the reaction at room temperature (2). After reaction completion, the OD405 absorbance was measured using the microplate reader. The enzyme activity was calculated using the equation above.

Bio-layer interferometry (BLI) and binding kinetics assays

Bio-layer interferometry (BLI) experiments were conducted using the BLItz/Octet N1 system with Anti-Penta-HIS (HIS1K) Biosensors (Sartorius, Goettingen, Germany). BLI is an optical detection technique that can determine the affinities of protein-ligand interactions on the sensor by reflecting a light beam.[60] STP protein with the hexahistidine (His_6) tags was attached to the fiber optic sensor tip with a selective tag immobilization method. The sensor tip was dipped into the small-molecule solution medium with a known concentration to load the small molecule ligands onto the sensor. The association of small molecules to the sensor represented by the association constant, k_a, causes the white light to shift in the interference pattern. The unbinding phenomenon, represented by the dissociation constant, k_d, will cause the white light to shift in

the opposite direction on the sensor. The dissociation/association ratio defines the affinity constant for the binding interactions (K_D) and is represented by the equation as follows:

$$K_D = \frac{[A]\cdot[B]}{[AB]} = \frac{k_d}{k_a}$$

Where K_D represents the affinity constants (M, or mol·L^{-1}), k_d represents the dissociation rate (s^{-1}), and k_a represents the association rate ($M\cdot s^{-1}$). Here, [A], [B], and [AB] represent the concentrations (M) of the unbound STP protein, small molecule ligands, and protein-ligand complex, respectively. The affinity constants will reveal the overall binding kinetics of the protein-ligand complex, which helps to evaluate the performance of the screened molecules.

The binding kinetics of *C*Lso and *C*Las STP and the screened molecules G6P6373 and G6P3510 were performed using recombinant STP proteins purified from *E. coli* and stored in 50 mM Tris-HCl, 500 mM NaCl, 10% Glycerol, 2 mM DTT, pH 8.0 buffer. The HIS1K sensors were hydrated in a 250 μL assay buffer for 30 minutes. The assay buffer was prepared with 9.95% 10X Pall Forte Bio kinetics buffer (Sartorius, Goettingen, Germany) and 89.55% PBS (Thermo Fisher Scientific, Waltham, MA), and 0.5% Dimethyl sulfoxide (DMSO) (Sigma-Aldrich, St. Louis, MO). The BLI test used a cycle of 30s assay buffer baseline, 300s STP protein loading, 120s baseline, 120s analyte association, and 120s analyte dissociation. The assay buffer was used in the two baseline and last dissociation phases. The concentration of protein and analytes was optimized for significant and measurable binding signals. For the *C*Las STP protein assay, 4 μL of *C*Las STP protein with 0.34 mg/ml concentration was loaded, and the testing analyte 1 μM G6P, 50 μM G6P6373, or 50 μM G6P3510 was associated in a 250 μL assay buffer, respectively. For the *C*Lso STP protein assay, 4 μL of *C*Las STP protein with 0.30 mg/ml concentration was loaded, and the testing analyte G6P, G6P6373, or G6P3510 was associated with 1 μM in a 250 μL assay buffer, respectively. All the BLItz experiments were conducted at room temperature. The Kinetics energies were analyzed in BLItz Pro 1.3.0.5 software (Sartorius, Goettingen, Germany) per manufacturer recommendations, and the interaction curves were exported from BLItz Pro and replotted with R studio.

In vitro and *in planta* efficacy trials

For the hairy root bioassays, *C*Lso-potato and *C*Las-citrus hairy roots were generated using *C*Lso- and *C*Las-infected plant tissues.[37] The presence of *C*Lso and *C*Las in the hairy roots was confirmed by qPCR amplification of the 16s rDNA[61] and *Ribonucleotide reductase β-subunit gene*, *nrdB* (RNR),[62] respectively (Table S2). The validated hairy roots were transferred to a multi-well titer plate containing Gamborg's B5 media. G6P3510 and G6P6373 inhibitors at 0, 5, 10, 20, and 50 μM were added, vacuum-infiltrated, and incubated for 72 hrs. Untreated and DMSO (0.1%) were used as negative controls, respectively. Three to five biological replicates were used for each treatment. After the treatments, tissue samples were treated with PMAxx (propidium monoazide) dye (Biotium, Fremont, CA) to inactivate dead bacterial DNA. Subsequently, total DNA was extracted, and quantitative PCR (qPCR) analysis was carried out to quantify the viable bacterial titers and plotted relative to the untreated controls (set to 100%) using the $^{\Delta\Delta}$Ct method.[63] After normalization of target Ct with an endogenous reference gene (Ct') to correct for DNA template concentration differences among the samples, it was plotted relative to untreated controls. The untreated was set to 100% for ease of visual representation.[37] Statistically significant differences among the controls and treatments were estimated using one-way ANOVA followed by a post-hoc LSD test (Figure 5). The *p* values were further corrected for multiple comparisons using the Benjamini-Hochberg (BH) FDR method.[64]

Non-target effects of G6P3510 and G6P6373 on unrelated bacteria were evaluated with *Pseudomonas syringae* pv. tomato DC3000 (*Pst*DC3000). DC3000 was cultured in a modified Luria-Bertani (LM) liquid medium either in the absence or presence of 5, 10, and 20 μM of G6P3510 and G6P6373 at 28 °C. Growth was recorded by measuring optical densities (OD 600 nm) at 0, 2, 4, 6, 8, 10, and 24 h and was converted to colony forming units (CFU)/80 μL.

For the in-planta trials, one-month-old potato plants (var. Atlantic) grown in a growth chamber at 21°C were challenged with 20 psyllids carrying *C*Lso. The challenged plants were maintained in secured cages to confine the insects to the plants. The psyllids were also restricted to two lower branches of the plant and contained using an organza drawstring bag tied around the branch. After one week, the bags containing psyllids were clipped off the plant to prevent the escape of the newly emerging psyllids and nymphs. All the challenged plants were sprayed with either 0, 10, and 50 μM of G6P3510 and G6P6373 (3-4 biological replicate plants/treatment) twice a week for up to four weeks.[37] The visual disease symptoms on the plants were monitored weekly, and tissue samples were collected at 28 days post-challenge for molecular diagnostics. Phytotoxicity assessments were performed similarly by treating healthy potato plants with 50 μM of G6P3510 and G6P6373 and monitoring visual symptoms of chlorosis, necrosis, or stunting.

For citrus treatments, four to five-month-old *C*Las-infected citron rooted plants maintained in the greenhouse were used for leaf infiltration. All the leaves of the plants were syringe-infiltrated[47] with either 0.1% DMSO (0.1%) solution or 100 μM solution of G6P3510 and G6P6373 (3 to 5 biological replicate plants/treatment) (Figure 8D). After 28 days, leaf tissues were sampled and subjected to genomic DNA isolation and qPCR molecular diagnostics.

DNA isolation and qPCR diagnostics

Total DNA was isolated from ~100 mg of tissue homogenized using Precellys 24 homogenizer (MO BIO Laboratories, Carlsbad, CA, USA).[65] The quality and quantity of DNA were determined using a NanoDrop 1000 Spectrophotometer (Thermo Fisher Scientific, Wilmington, DE, USA) and by agarose gel electrophoresis. Approximately 50 ng of total DNA was used for qPCR analysis, performed on a CFX384™ Real-Time PCR Detection System (Bio-Rad Laboratories, Inc., Hercules, CA, USA) using iTaq™ universal SYBR® Green supermix (Bio-Rad

Laboratories, Inc.), following the manufacturer's instructions. The 16s rDNA Lso-F and HLB-R primers were utilized for *C*Lso detection,[61] while *RNR* primers were used for *C*Las detection[62] (Table S2). A dissociation melting curve analysis showed no non-specific amplification or primer dimers. Relative *C*Lso and *C*Las titers were estimated using the $^{\Delta\Delta}$Ct method.[63] The *C*Lso and *C*Las Ct values were normalized to *RIBOSOMAL PROTEIN L2 (StRPL2)* and the citrus *GLYCERALDEHYDE-3-PHOSPHATE DEHYDROGENASE C2 (GAPC2)* to correct for DNA template concentration differences among the samples. They were plotted relative to the untreated controls, which were set to 100%.

QUANTIFICATION AND STATISTICAL ANALYSIS

All the data analysis, statistics, and graphs were displayed using Microsoft Excel software (version 2009) and the Python bioinfokit package (https://github.com/mandadi-lab/bioinfokit). The graphical abstract was created with Biorender (https://BioRender.com).